

# JGR Solid Earth

## RESEARCH ARTICLE

10.1029/2020JB019794

### Key Points:

- High-frequency *S* coda and long-period Rayleigh waves from repeating earthquakes reveal velocity changes since the 2004 Sumatra earthquake
- *S* coda velocity changes underwent steady recovery from 2005 to 2015, while Rayleigh wave velocities decreased significantly in late 2007
- Temporal differences in *S* coda and Rayleigh velocity changes can delineate slow deformation at depth and healing of the surface damage zone

### Supporting Information:

- Supporting Information S1

### Correspondence to:

W. Yu,  
fgsyw@earth.sinica.edu.tw

### Citation:

Yu, W., Lin, J.-T., Su, J., Song, T.-R. A., & Kang, C.-C. (2020). *S* coda and Rayleigh waves from a decade of repeating earthquakes reveal discordant temporal velocity changes since the 2004 Sumatra earthquake. *Journal of Geophysical Research: Solid Earth*, 125, e2020JB019794. <https://doi.org/10.1029/2020JB019794>

Received 16 MAR 2020

Accepted 12 MAY 2020

Accepted article online 19 MAY 2020

## S Coda and Rayleigh Waves From a Decade of Repeating Earthquakes Reveal Discordant Temporal Velocity Changes Since the 2004 Sumatra Earthquake

W. Yu<sup>1</sup> , J.-T. Lin<sup>2</sup> , J. Su<sup>1</sup> , T.-R. A. Song<sup>3</sup> , and C.-C. Kang<sup>4</sup> 

<sup>1</sup>Institute of Earth Sciences, Academia Sinica, Taipei, Taiwan, <sup>2</sup>Department of Earth Sciences, University of Oregon, Eugene, OR, USA, <sup>3</sup>Department of Earth Sciences, University College London, London, UK, <sup>4</sup>Department of Natural Sciences and Sustainable Development, Ministry of Science and Technology, Taipei, Taiwan

**Abstract** Temporal changes in the subsurface seismic velocity structure reflect the physical processes that modulate the properties of the media through which seismic waves propagate. These processes, such as healing of the surface damage zone and deep crustal deformation, are described by similar functional forms and operate on similar timescales, making it difficult to determine which process drives the observed changes. We examine earthquake-induced velocity changes using the measured lag-time time series  $\tau(t)$  of the repeating earthquake sequences since the 2004  $M_w$  9.2 Sumatra and 2005  $M_w$  8.6 Nias earthquakes. The *S* coda velocity changes ( $\delta V_S$ , equivalent to  $-\tau_S$ ) recover steadily during the 2005–2015 period. The Rayleigh wave velocity changes ( $\delta V_{LR}$ , or  $-\tau_{LR}$ ) undergo transient recovery, followed by a strong  $\delta V_{LR}$  reduction in late 2007.  $\delta V_S$  recovery is most likely driven by deep processes, whereas the temporal breaks in  $\delta V_{LR}$  recovery in 2007 mostly reflect surface damage and healing induced by the strong ground motions of the 2004  $M_w$  9.2, 2005  $M_w$  8.6, 2007  $M_w$  8.4, and  $M_w$  7.9 Bengkulu and 2008  $M_w$  7.3 Simeulue earthquakes. The observed differences between the temporal variations in  $\delta V_S$  and  $\delta V_{LR}$  can distinguish deep processes from healing of the surface damage zone.

**Plain Language Summary** Earthquake slip leads to stress relaxation in the crust, whereas healing of the damage induced by strong ground motion predominantly occurs in the near surface. Temporal changes in the seismic velocity structure after large earthquakes can be driven by diverse mechanisms, such as aseismic slip or fault zone healing, but the timescales governing these processes are very similar, making them difficult to distinguish. We detect temporal velocity changes in the crust since the great 2004 Sumatra and 2005 Nias earthquakes using the high-frequency late-arriving scattered waves after the *S* phase and long-period Rayleigh waves of repeating earthquakes. We find that the temporal velocity changes in the scattered waves exhibit steady logarithmic recovery from 2005 to 2015, whereas the Rayleigh wave velocity recovery was interrupted by several large earthquakes after late 2007. The difference between these two temporal trends in velocity change is the key to distinguishing between a damage/healing/redamage cycle near the surface and slow deformation (e.g., afterslip and postseismic relaxation) at depth. Rayleigh waves are highly sensitive to the near-surface damage and healing after the 2004/2005 events and also the repeated damage induced by the 2007 and 2008 earthquakes. Steady velocity recovery of the scattered waves primarily corresponds to slow deformation at depth.

## 1. Introduction

Long-term monitoring of temporal seismic-velocity variations in the crust is an important and long-sought goal in geophysics because these temporal changes can be proxy measures for the mechanical processes and timescales of crustal responses to earthquake slip. Numerous studies have suggested that these temporal velocity changes are often associated with the peak ground velocity (PGV) or acceleration (PGA) that is induced by the strong ground motion (GM) of an earthquake (Hobiger et al., 2016; Rubinstein & Beroza, 2004a; Rubinstein et al., 2007; Schaff & Beroza, 2004; Takagi et al., 2012; Wegler et al., 2009; T. Yu & Hung, 2012; Y.G. Li et al., 2006). Strong GM damages the subsurface sediment layer, which is subjected to low confining pressures of only a few tens of MPa (L. Li et al., 2017; Sawazaki et al., 2015; Wu et al., 2009; Zhao & Peng, 2009). The subsequent velocity recovery, which probably reflects healing of the subsurface damage zone, is typically characterized by a logarithmic time dependence (so-called “slow dynamics”) (Brenguier et al., 2008; Peng & Ben-Zion, 2006; Snieder et al., 2017; TenCate et al., 2000).

©2020. The Authors.

This is an open access article under the terms of the Creative Commons Attribution License, which permits use, distribution and reproduction in any medium, provided the original work is properly cited.

Similar pattern of temporal velocity changes may also be associated with aseismic slip (or slip rate), postseismic afterslip (Rivet et al., 2011; Yu et al., 2013a) and viscoelastic relaxation in the bulk crust. Postseismic transients due to afterslip and dilatancy recovery occur adjacent to the earthquake slip zone and can modulate the crack density and pore pressure, yielding recoveries in *S* wave velocity and Poisson's ratio (Fialko, 2004; Fielding et al., 2009; Peltzer et al., 1996). Viscoelastic relaxation mainly occurs in the lower crust and upper mantle over longer timescales and can restore the stress perturbation induced by coseismic slip (Barbot & Fialko, 2010; Qiu et al., 2018; Tang et al., 2019). Postseismic transient processes due to dilatancy recovery (Fialko, 2004; Jónsson et al., 2003), afterslip (Froment et al., 2013), and viscoelastic relaxation all follow similar logarithmic decay patterns. However, it is difficult to unambiguously associate an observed logarithmic velocity recovery with a specific physical mechanism and/or depth (Obermann et al., 2016, 2013; Yang et al., 2019) since all of the processes that influence the subsurface damage zone and postseismic transients operate on similar timescales. For example, both the healing of the fault zone (Y. G. Li et al., 1998) and decay of postseismic deformation (Fialko, 2004) are prominent over several years after the 1992  $M_w$  7.3 Landers earthquake.

W. Yu et al. (2013b, 2013a) detected repeating earthquakes (REs) near the Sumatra Subduction Zone and used these repeaters to probe the temporal changes in seismic velocity induced by the 2004  $M_w$  9.2 Sumatra and 2005  $M_w$  8.6 Nias earthquakes during 2005–2008. They found that the temporal velocity changes in the high-frequency (HF, 0.5–2.0 Hz) *S* wave coda ( $\delta V_S$ ) and long-period (LP, 0.03–0.1 Hz) Rayleigh waves ( $\delta V_{LR}$ ) followed similar logarithmic recovery timescales after the 2004 and 2005 earthquakes that were potentially linked to strong GM-induced surface damage or/and postseismic afterslip. However, the ability to distinguish the velocity changes induced by deep processes from healing of the subsurface damage zone remains a challenge, as mentioned above.

Cracks produced by a previous earthquake can multiply within the subsurface damage zone as a result of the strong GM induced by subsequent earthquakes (Rubinstein & Beroza, 2004a). If the logarithmic velocity recovery reflects healing of the subsurface damage zone, then the redamage process from subsequent large earthquakes could result in further reduction of the seismic velocity, reversing the established recovery pattern (Rubinstein & Beroza, 2004a; Sawazaki et al., 2018; Vidale & Li, 2003). However, velocity recovery is likely to continue without reversal if it is driven by postseismic afterslip or other deep processes, even in the event of another earthquake. Therefore, the ability to detect such a bifurcation in the temporal velocity recovery patterns would help discriminate between the healing of surface damage zones and slow deformation in the crust.

The 2004  $M_w$  9.2 Sumatra earthquake (Ammon et al., 2005; Chlieh et al., 2007; Park et al., 2005; Subarya et al., 2006) has been followed by a series of large earthquakes that have occurred in the proximity of the 2004 rupture zone and in the Wharton Basin, northeast Indian Ocean (Figure 1; see Table S1 in the supporting information for the event IDs). Examples of the former include the 2005  $M_w$  8.6 Nias earthquake (Hsu et al., 2006; Ishii et al., 2007; Konca et al., 2007), 2007  $M_w$  8.4 and  $M_w$  7.9 Bengkulu double earthquakes (Konca et al., 2008; Tsang et al., 2016), 2008  $M_w$  7.3 Simeulue earthquake (Morgan et al., 2017), and 2010  $M_w$  7.8 Banyak earthquake, and examples of the latter include the 2012  $M_w$  8.6 and  $M_w$  8.2 double earthquakes (Hill et al., 2015; H. Yue et al., 2012; Wei et al., 2013). The strong GM generated by these large earthquakes can repeatedly damage the surface layer and interrupt healing, whereas the large postseismic afterslip from the 2004  $M_w$  8.8 Sumatra and 2005  $M_w$  8.2 Nias events (Chlieh et al., 2007; Feng et al., 2015; Hoechner et al., 2011; Hsu et al., 2006) (Figure 1), among other slow deformation processes, potentially drives continuous velocity changes. The main goal of this work is to examine how seismic-velocity change measurements from different attributes can help differentiate between these concurrent processes.

We extend our previous work (W. Yu et al., 2013a) by incorporating seven additional years of regional seismic waveform data, which expands our RE data set to the 2005–2015 time period. We discuss the data processing procedures and summarize the observed temporal velocity changes in  $\delta V_S$  and  $\delta V_{LR}$  in the following sections, where we highlight a clear bifurcation in the  $\delta V_S$  and  $\delta V_{LR}$  patterns:  $\delta V_S$  follows a monotonic logarithmic recovery, while  $\delta V_{LR}$  deviates from the background recovery rate in late 2007. Through a forward modeling approach, we explore a series of perturbed velocity models and examine the sensitivity of these models against the observed attributes, to reconcile the first-order pattern shown in the observed lag-time time series  $\tau(t)$  of the HF *S* coda and LP Rayleigh waves.

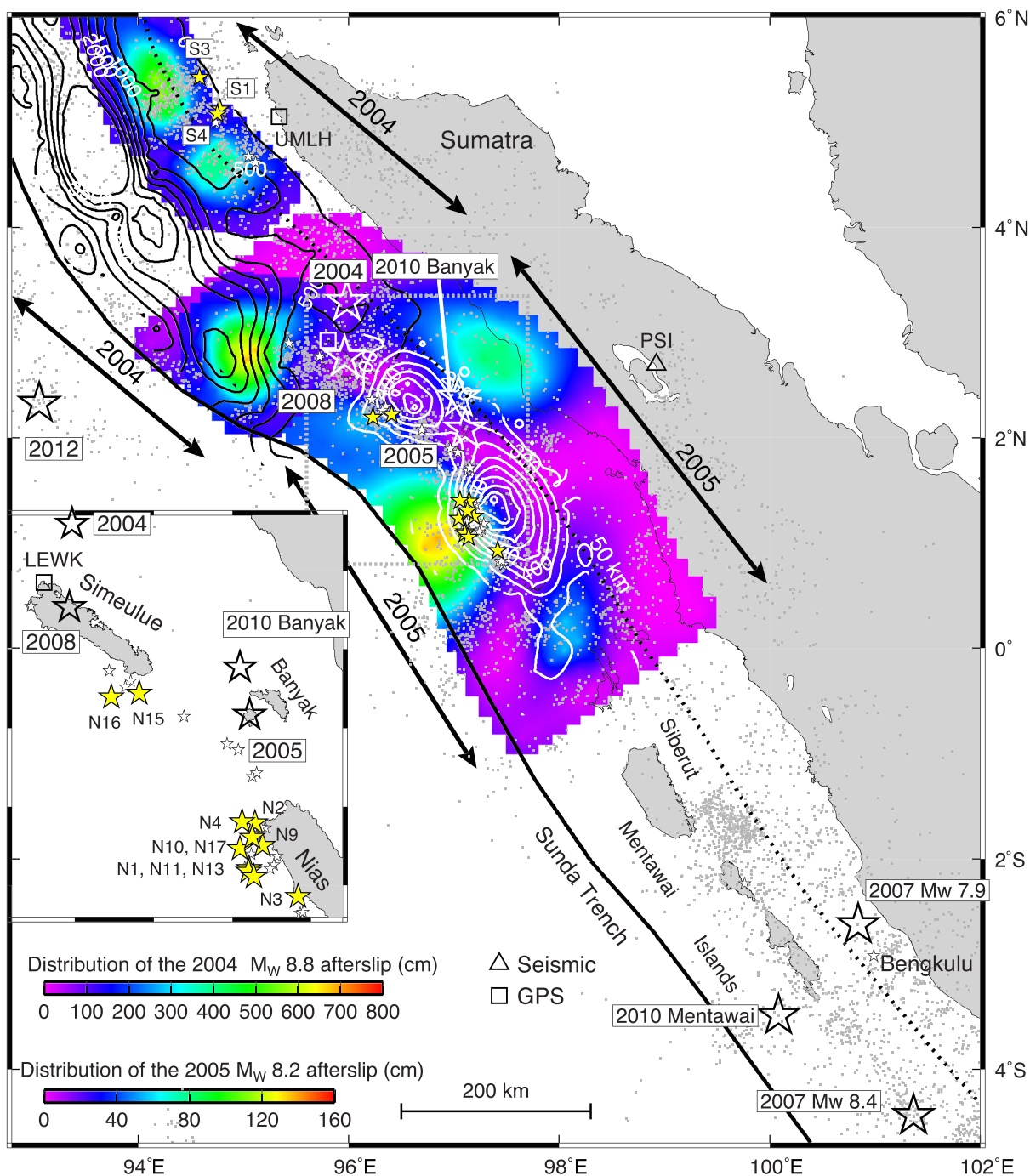


**Figure 1.** Regional seismicity map of the Sumatra Subduction Zone. The epicenters of several major earthquakes ( $M_w \geq 7.3$ ) are shown as either large open white or black stars that are labeled with their respective event ID or  $M_w$  values, respectively (Table S1). The repeating earthquake (RE) sequences are represented by small stars, and the background seismicity is represented by the gray dots, all of which is superimposed on the modeled coseismic slip (contours) and postseismic afterslip (colored area) of the 2004 Sumatra (Chlieh et al., 2007) and 2005 Nias (Hsu et al., 2006) earthquakes. Note that color scales for the afterslip values of the 2004 and 2005 events are different. The double arrows show the rupture extents of the 2004 and 2005 events on the map. The REs that were selected for the relative locations and temporal velocity change analyses (Table S2) are indicated by small yellow stars, whereas the REs with high cross-correlation (CC) coefficients and no further relocation analysis are indicated by small white stars; the source parameters of the latter are not provided. The REs are located near the afterslip zones of the 2004 and 2005 events (Chlieh et al., 2007). The solid and dotted black lines indicate the trench (Bird, 2003) and slab depths at 50-km intervals (Gudmundsson & Sambridge, 1998), respectively. The seismic and GPS stations used in this analysis are indicated by the open triangle and open squares, respectively. An enlarged map near the Nias, Banyak, and Simeulue Islands is provided to better present the 2005 Nias earthquake RE locations, with the dotted gray box indicating the location of the displayed region in the main figure.

## 2. Seismic Data and $\tau(t)$ and $\delta V$ Measurements

### 2.1. REs Recorded by Seismographic Station PSI

The procedural details for the RE detection and relative location assessment within a given earthquake sequence have been discussed in previous studies (Wen, 2006; W. Yu, 2013; W. Yu et al., 2013b; W. Yu & Wen, 2012). Several previously identified RE sequences continued to occur in the afterslip zones of the 2004 and 2005 earthquakes until the end of 2015 (Figure 1). The high-precision relative hypocenter locations of these REs (relative to the estimated rupture area of the selected RE sequences) are presented in the supporting information (Text S1, Figure S1, and Table S2). Seismographic station PSI, which was installed in Parapat, Sumatra, Indonesia, in 1993, is equipped with a Streckeisen STS-2 broadband sensor. Station PSI detected the REs immediately after the 2004 and 2005 mainshocks, and it is in an advantageous position to potentially detect the  $\delta V$  induced by the 2005 event since the seismic waves from the RE sequences associated with the 2005 event propagated through the main slip and surface damage zones of the 2005 event as they traveled to station PSI.

### 2.2. $\tau(t)$ Measurements Using Coda Wave Interferometry

Coda wave interferometry is used to measure the  $\tau(t)$  of the HF S coda and LP Rayleigh waves relative to the direct  $P$  wave onset in a given RE sequence (Poupinet et al., 1984; Snieder, 2006; Snieder et al., 2002). The HF waveforms are convolved using a zero-phase two-pole Butterworth band-pass filter with 0.5-and 2.0-Hz corner frequencies, and the LP Rayleigh waves are band-pass filtered between 0.03 and 0.1 Hz. The reference event of a given RE sequence is chosen as the last event before late 2007, when the onset of an additional increase in the Rayleigh wave lag times ( $\tau_{LR}$ ) is detected (to be discussed in section 3). We measure the differential time of the first 4-s HF  $P$  wave between the target and reference events via the cross correlation (CC) of each RE pair. We adopt 4- and 40-s sliding windows for the HF coda and LP surface waves, respectively, with a 95% overlap between successive time windows for both waves. The  $\tau(t)$  for the HF S coda and LP Rayleigh waves are computed as the time differences between either the HF S coda or LP Rayleigh waves, and the HF  $P$  wave onset using a sliding-window CC approach. We emphasize that a 40-s time window is sufficient to include the entire cycle of a 20-s period Rayleigh wave packet. A 50-ms sampling interval of the original time series is interpolated to a 5-ms sampling interval to achieve subsample precision in time, which can alternatively be attained by interpolating the resulting CC time series. We find that the  $\tau(t)$  calculated via CC of the interpolated time series is identical to that obtained via interpolation of the resulting CC time series. The  $\tau(t)$  for the HF S coda waves ( $\tau_S$ ) can be expressed as follows:

$$\tau_S = \left( t_{S \text{ coda}}^{\text{trg}} - t_{S \text{ coda}}^{\text{ref}} \right) - \left( t_{\text{HF } P}^{\text{trg}} - t_{\text{HF } P}^{\text{ref}} \right), \quad (1)$$

where  $t$  refers to the arrival times (or lapse times) of the initial 4-s HF  $P$  (subscripted “HF  $P$ ”) and S coda (subscripted “S coda”) waves between the target (superscripted “trg”) and reference (superscripted “ref”) events of a given RE pair. The  $\tau(t)$  for the 20-s dominant period long-period (LP) Rayleigh waves ( $\tau_{LR}$ ) can be expressed as follows:

$$\tau_{LR} = \left( t_{20s \text{ LR}}^{\text{trg}} - t_{20s \text{ LR}}^{\text{ref}} \right) - \left( t_{\text{HF } P}^{\text{trg}} - t_{\text{HF } P}^{\text{ref}} \right). \quad (2)$$

The  $\tau(t)$  measurements can eliminate the uncertainties due to the relative origin time error of the event catalog and Global Positioning System (GPS) clock drift error between the two events in a given RE pair.  $\tau(t)$  at the HF  $P$  wave onset ( $\tau_P$ ) is negligible due to media velocity changes because the waves are aligned relative to the direct  $P$  wave onset. Figures 2a and 2c display example HF coda and LP Rayleigh waveforms from the N1 RE sequence that were recorded by station PSI, respectively, with the waveforms of the target events aligned via CC of the 4-s HF  $P$  wave between the target and reference events. Time zero in Figures 2a and 2c refer to the HF  $P$  wave onset and event origin time of the reference event, respectively. Figures 2b and 2d display the calculated  $\tau(t)$  of the HF coda and LP Rayleigh waves from the corresponding waveforms displayed in Figures 2a and 2c, respectively. Signal-to-noise ratios (SNRs) are used to sort the time segments with sufficient signal strength and are defined as follows: The noise amplitude is measured as the maximum amplitude in the 5- to 15-s time window before the  $P$  wave arrival, and the signal amplitude is measured as the maximum amplitude in a given time window. W. Yu et al. (2013a) previously adopted SNR thresholds of

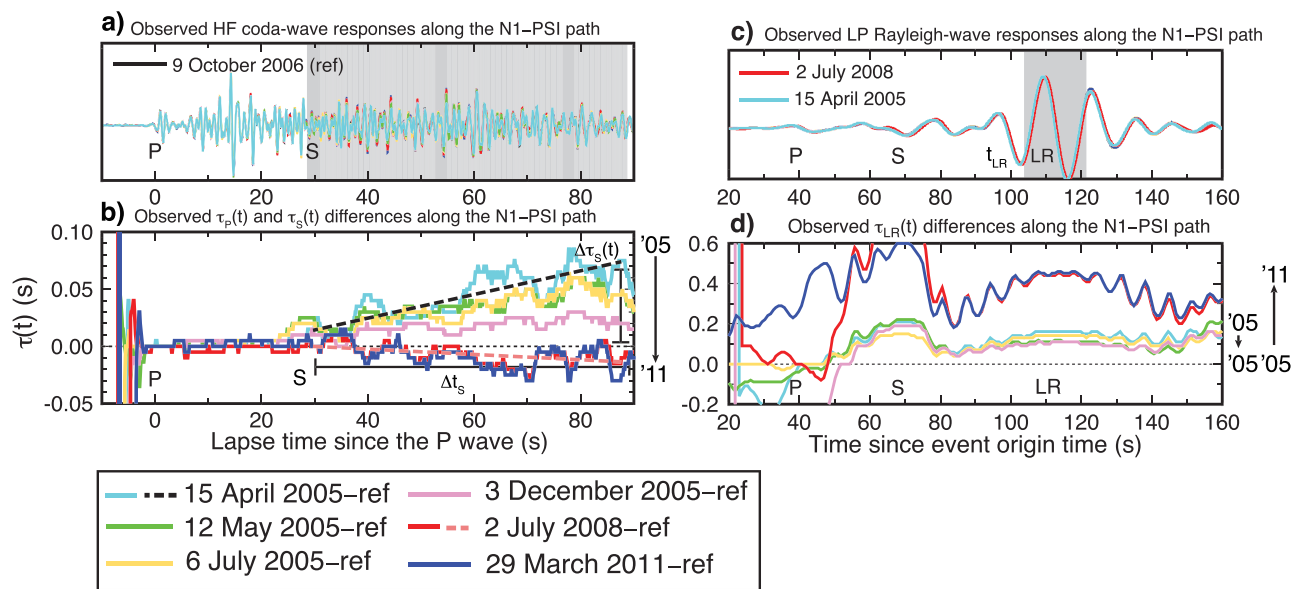


**Figure 2.** (a, c) Waveforms and (b, d) lag-time time series  $\tau(t)$  for the N1 RE sequence recorded at Station PSI. The vertical-component data are shown for the (a, b) high-frequency (HF) coda waves, band-pass filtered between 0.5 and 2.0 Hz, and (c, d) long-period (LP; 0.03–0.1 Hz) Rayleigh waves. HF waveforms and  $\tau(t)$  are aligned relative to the HF direct  $P$  wave onset in (a) and (b), whereas LP Rayleigh waves and  $\tau_{LR}(t)$  are aligned relative to origin time of the reference event in (c) and (d). The  $\tau(t)$  values for the target event are computed relative to the reference event (black trace, 9 October 2006) and labeled “target event ID-ref.” The amplitudes of the filtered waveforms in each selected time window are normalized to the maximum amplitude in that window. The shaded regions correspond to the waveform segments with signal-to-noise ratios (SNR) of  $\geq 5$  and cross-correlation (CC) coefficients of  $\geq 0.9$ , which are used to compute  $\delta V$ . The unstable and oscillatory  $\tau(t)$  values at the beginning of each lower plot are due to low SNR values. The dashed black and light-red lines in (b) correspond to the  $-\delta V_S$  values that are estimated from the observed slope of  $\Delta\tau_S(t)$  over  $\Delta t_S$  of the target events: 15 April 2005 (light-blue line) and 2 July 2008 (red line), respectively. The arrival times of the  $P$ ,  $S$ , and LP Rayleigh waves are labeled “ $P$ ,” “ $S$ ,” and “LR” (“ $t_{LR}$ ”), respectively.

5 for HF  $S$  coda waves and 10 for LP Rayleigh waves. However, a minimum threshold of  $\text{SNR} = 10$  with this new data set would exclude many  $\tau_{LR}$  measurements, yielding few temporal samples for the RE sequences. Therefore, we explore suitable SNR thresholds for the LP Rayleigh waves of smaller events. We find that a threshold requiring at least 80% of the 40-s lapse time segments to satisfy SNR of  $\geq 5$  and a CC coefficient of  $\geq 0.9$  between each waveform pair yields a reasonable number of  $\tau_{LR}$  measurements and stable  $\tau_{LR}$  values. We acquire 471  $\tau(t)$  measurements from the HF  $S$  coda and LP Rayleigh waves using the above-mentioned SNR and CC thresholds.

### 2.3. $\delta V_S$ and $\delta V_{LR}$ Measurements and Uncertainties

The observed  $\tau_S(t)$  for the 2005 Nias earthquake RE sequences is stretched in the later part of the coda waves (see section 3), similar to previous findings (Lobkis & Weaver, 2003; Poupinet et al., 1984). A fractional seismic-velocity change in the  $S$  wave coda ( $\delta V_S$ ) of the RE pair can be approximated by a negative  $\tau_S(t)$  slope (dashed lines in Figure 2b).

$$\delta V_S = -\frac{\Delta\tau_S(t)}{\Delta t_S}, \quad (3)$$

where  $\Delta t_S$  is the lapse time difference between the  $S$  wave coda at lapse time  $t$  and the  $S$  wave onset, with the corresponding lag time difference  $\Delta\tau_S(t)$ .  $\delta V_S$  is computed from the negative slope of time delays of the  $S$  codas that yields a path-averaged value (Poupinet et al., 1984; Rubinstein et al., 2007; Sawazaki et al., 2015; Schaff & Beroza, 2004). Linear regression is used to estimate the parameters of the slope  $b$  ( $-\delta V_S$ ) and intercept  $a$  whose  $\tau_S$  values that meet the SNR and CC coefficient thresholds. The  $2\sigma$  standard deviations in  $\delta V_S$  are twice the computed root-mean-square (RMS) of  $\tau_{IS} - \hat{\tau}_{IS}$ , where  $\hat{\tau}_{IS} = a + b\Delta t_S$ , which is the predicted value based on the inferred  $a$  and  $b$  values. However,  $\tau_{LR}$  is nearly

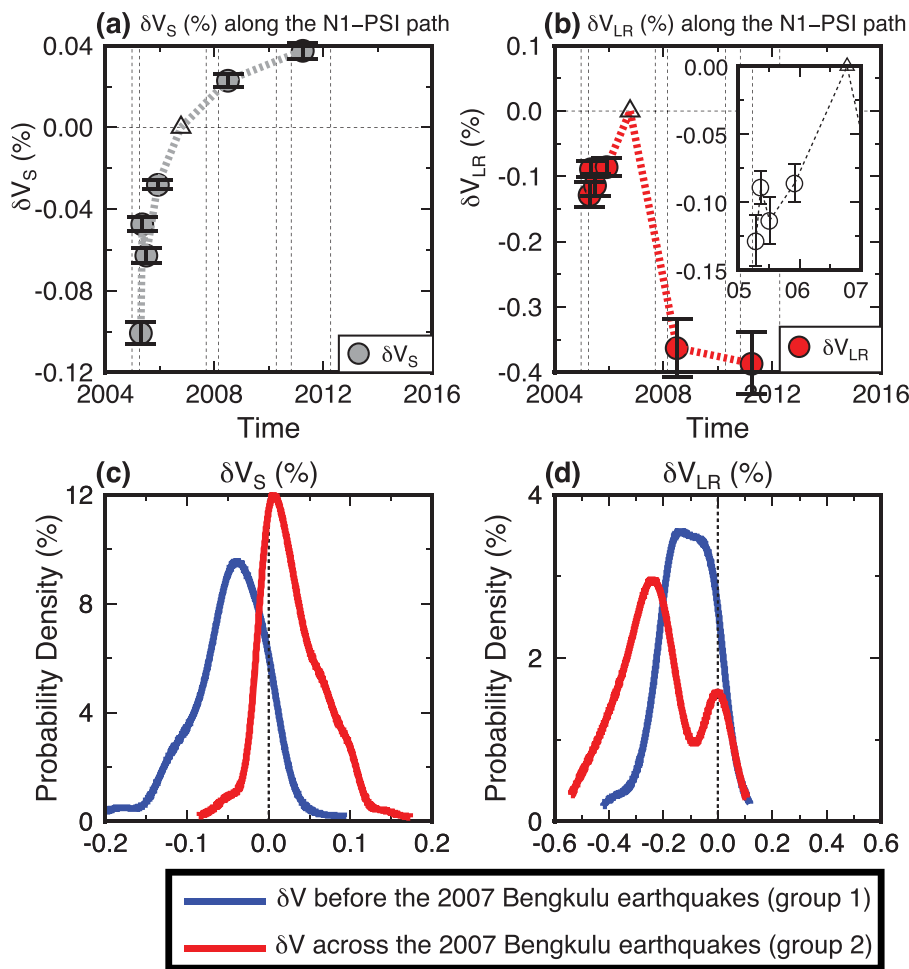


**Figure 3.** Temporal velocity changes in (a)  $\delta V_S$  and (b)  $\delta V_{LR}$ , and their respective standard deviations (error bars) for the N1 RE sequence recorded at station PSI during the 2005–2011 time period, beginning after the 2005 event. The reference event is indicated by the open black triangle and placed on the zero line (baseline). The  $2\sigma$  standard deviations in  $\delta V_S$  and  $\delta V_{LR}$  are discussed in the text. The vertical dotted lines correspond to the major earthquakes near the Sumatra Subduction Zone, including the 2004, 2005, 2007, 2008, and 2010 Banyak, 2010 Mentawai, and 2012 earthquakes (earthquake details listed in Table S1). In (b), an enlarged view is displayed in the inset to better present the recovery of  $\delta V_{LR}$  (open circles) during the 2005–2006 time period. The (c)  $\delta V_S$  and (d)  $\delta V_{LR}$  distributions, measured from the REs that have been relocated (Table S2) and possess high CC coefficients, and determined using Equations 5 and 6. The contrast in  $\delta V$  before and across the 2007 Bengkulu earthquakes, which is inferred from the probability density function for all of the data, resembles the  $\delta V$  distributions constructed from the individual RE sequences.

constant for the entire wave packet (Figure 2d). The fractional velocity change for the LP Rayleigh wave ( $\delta V_{LR}$ ) is computed as follows:

$$\delta V_{LR} = -\frac{\bar{\tau}_{LR}}{t_{LR}}, \quad (4)$$

where  $\bar{\tau}_{LR}$  is the mean of the  $\tau_{LR}$  whose lapse time segments that satisfy the SNR and CC coefficient thresholds and  $t_{LR}$  is the Rayleigh wave absolute arrival time (Figure 2c). The  $2\sigma$  standard deviations in  $\delta V_{LR}$  are twice the computed RMS of  $\tau_{i,LR} - \bar{\tau}_{LR}$  (Figure 3 and the following figures).

We emphasize that  $\delta V_S$  and  $\delta V_{LR}$  are used to highlight the time-dependent discrepancy in late 2007. If the upper crust experiences partial or uniform velocity perturbations induced by earthquake slip, then one would anticipate detectable changes in the direct S wave and in both the P and S coda waves. We observe that the  $\tau_P$  values are smaller than the  $\tau_S$  values and only detectable immediately after the Nias earthquake (see section 3). Therefore, we only focus on  $\delta V_S$  and  $\delta V_{LR}$  in our analysis. We consider the effect of fractional

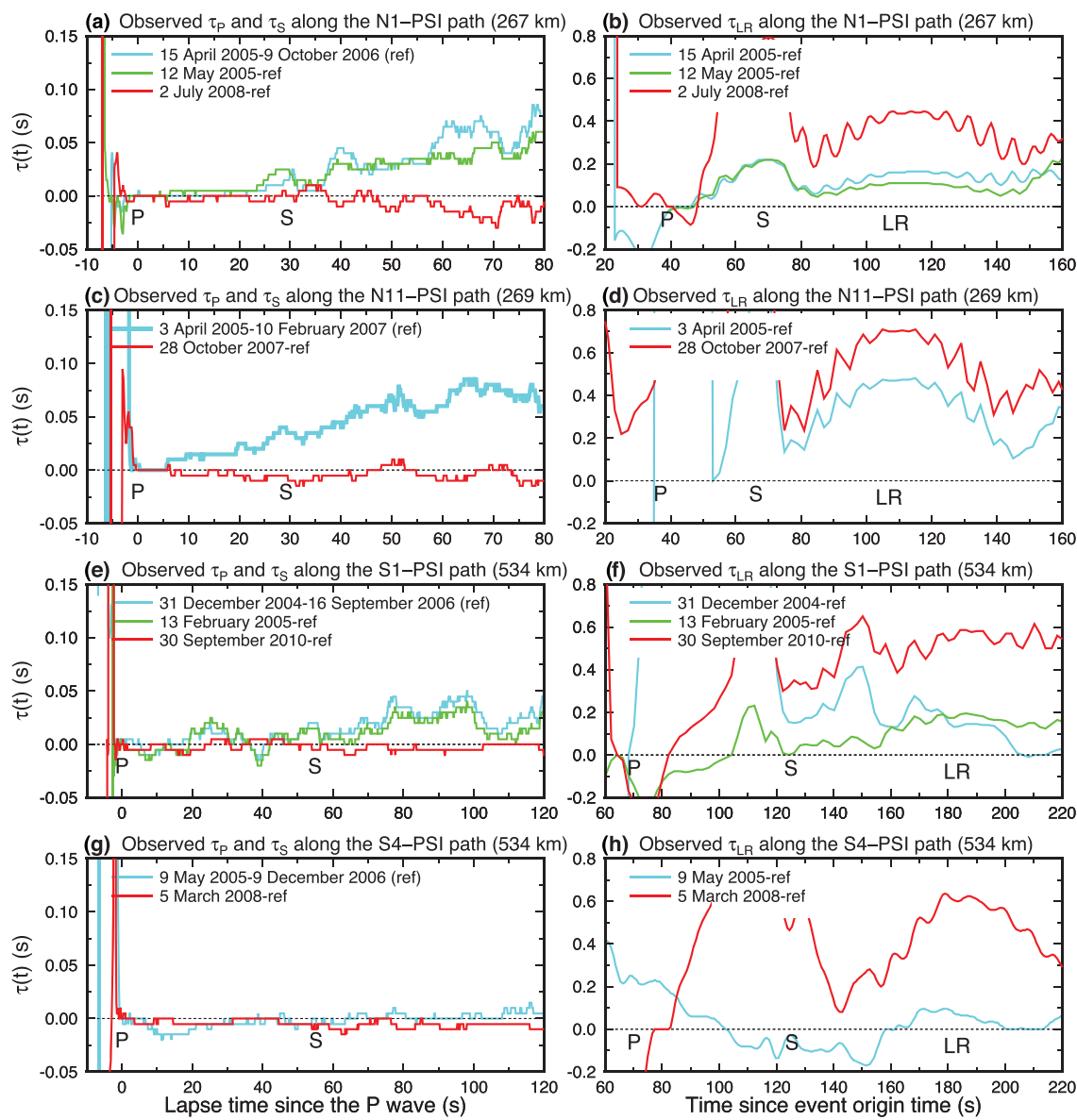


**Figure 4.** Observed  $\tau(t)$  for the selected target events from four RE sequences, recorded at station PSI: (a, b) N1, (c, d) N11, (e, f) S1, and (g, h) S4. The HF  $\tau_P$  and  $\tau_S$  (left panels) and LP  $\tau_{LR}$  (right panels) are aligned relative to the HF  $P$  wave onset and origin time of the reference event. The epicentral distance between each RE sequence and station PSI (in km) is displayed in the titles. The light-blue and green curves are the measured  $\tau(t)$  for the target events that occurred after the 2004 and 2005 earthquakes, whereas the red curve is the measured  $\tau(t)$  for the target events that occurred after the 2007 and 2008 earthquakes. The measured  $\tau(t)$  for the 3 April 2005 target event of the N11 sequence in (c) indicates detectable  $\tau_P$  and  $\tau_S$  at the  $S$  wave onset that are highlighted by the thick light-blue curve. This figure is similar to Figures 2b and 2d.

changes in both the  $P$  and  $S$  wave velocities of the crust and how the velocity model perturbations influence the synthetic  $\tau(t)$  results (see section 4).

### 3. Temporal Changes in $\delta V_S$ and $\delta V_{LR}$ : Observations of Bifurcation

We examine the  $\tau_S(t)$  from the N1 sequence at station PSI to determine the decade-long temporal evolution of  $\delta V_S$  and  $\delta V_{LR}$  (Figures 2 and 3). The  $\tau_S$  values of the first target event (15 April 2005) increase monotonically to  $\tau_S = +0.07$  s (light-blue curve in Figure 2b) relative to the 9 October 2006 reference event, which is equivalent to  $\delta V_S = -0.1\%$  (dashed black line in Figure 2b). The slope of  $\tau_S$  decreases with time. However, the  $\tau_S$  values for the 2 July 2008 target event decrease to about  $-0.02$  s (red curve in Figure 2b), which is

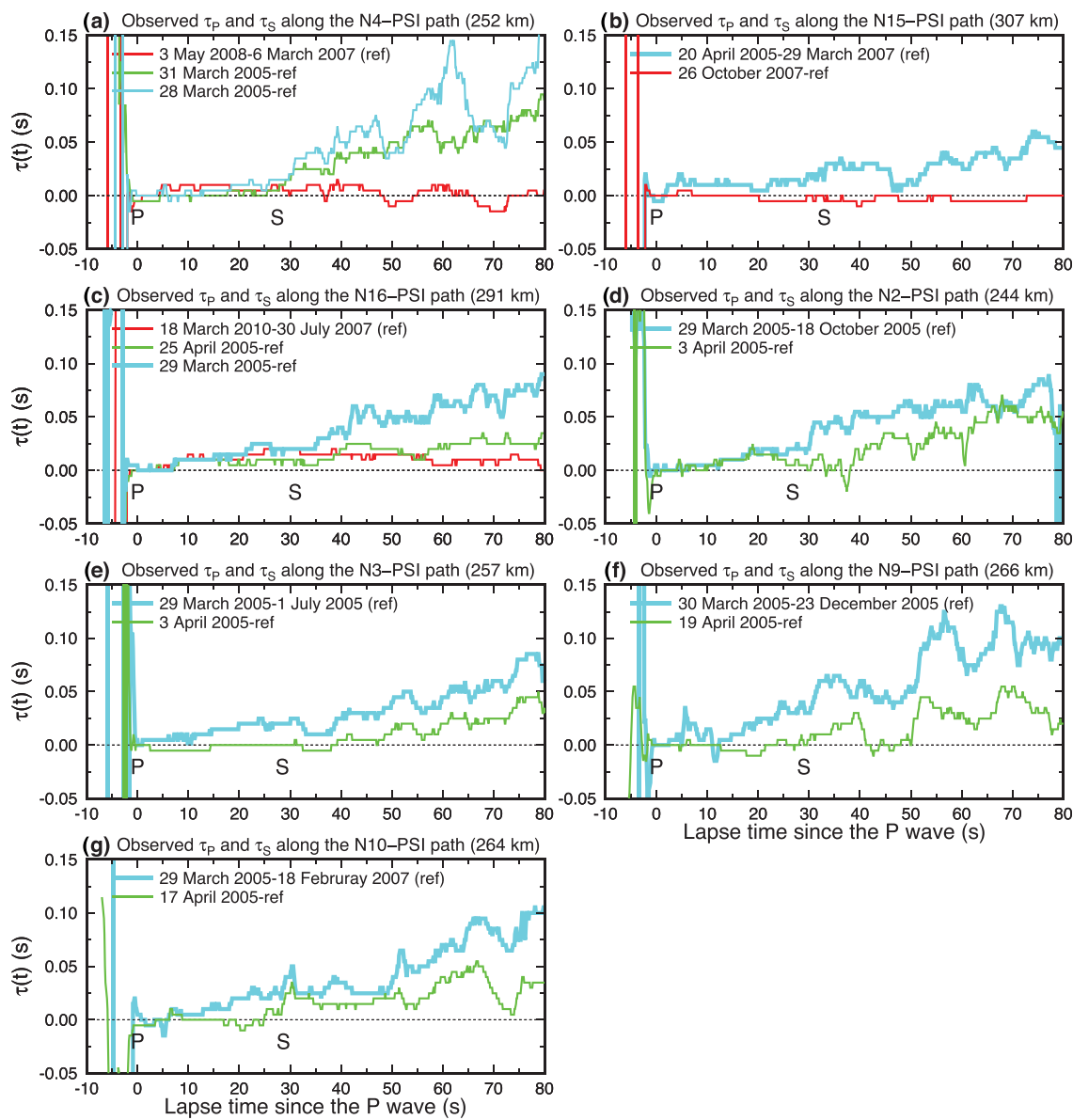


**Figure 5.** Observed  $\tau(t)$  of the HF coda waves for the selected target events from seven Nias RE sequences recorded at station PSI: (a) N4, (b) N15, (c) N16, (d) N2, (e) N3, (f) N9, and (g) N10. The thick light-blue curves indicate detectable  $\tau_P$  and  $\tau_S$  at the S wave onset, which are mostly detectable for the target events that occurred within the first week following the 2005 Nias earthquake. This figure is similar to Figures 4a, 4c, 4e, and 4g.

equivalent to  $\delta V_S = +0.02\%$  (dashed light-red line).  $\delta V_S$  exhibits a continuous recovery between 2005 and 2011 that amounts to  $\sim 0.14\%$  (Figure 3a).

The  $\tau_{LR}$  value for the first target event (15 April 2005) is about  $+0.16$  s (light-blue curve in Figure 2d) and then decreases to  $+0.11$  s for the 3 December 2005 event. However, the  $\tau_{LR}$  values increase to  $+0.44$  s for the subsequent 2 July 2008 and 29 March 2011 target events (red and blue curves in Figure 2d, respectively).  $\delta V_{LR}$  recovered from  $-0.13\%$  to  $-0.09\%$  between 15 April and 3 December 2005 but then decreased to  $-0.36\%$  between 9 October 2006 and 2 July 2008, which is almost 3 times greater than the change in  $\delta V_{LR}$  in the 3 weeks following the 2005 Nias mainshock (Figure 3b). The  $\tau_{LR}$  amplification after 2007 is detected in other band-pass-filtered frequency range of 20–30, 16–24, and 12–18 s as well (Figures S2 and S3 in the supporting information). These observations therefore include a clear break from the observed recovery trend after late 2007.

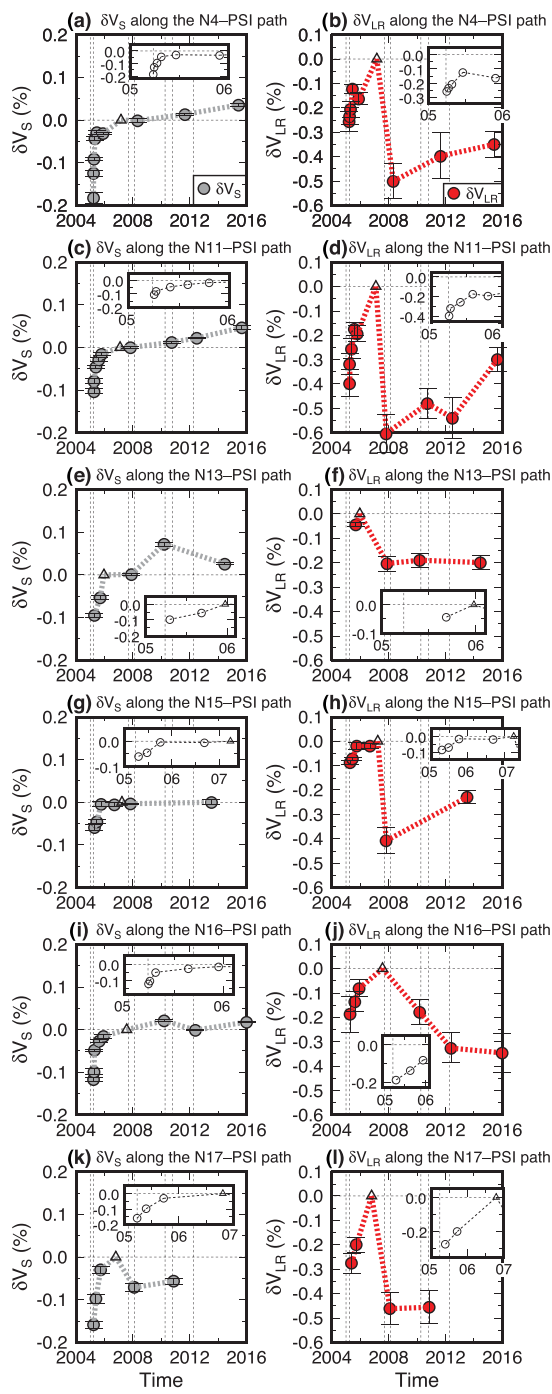


**Figure 6.** Temporal  $\delta V_S$  (gray circles) and  $\delta V_{LR}$  (red circles), and their respective standard deviations (black error bars) for six Nias RE sequences recorded at station PSI: (a, b) N4, (c, d) N11, (e, f) N13, (g, h) N15, (i, j) N16, and (k, l) N17, displayed over the 2005–2015 time period to highlight the consistency in both the  $\delta V_S$  recovery and temporal break in  $\delta V_{LR}$  recovery after late 2007. The vertical dotted lines indicate the origin times of the 2004, 2005, 2007, 2008, and 2010 Banyak, 2010 Mentawai, and 2012 earthquakes (Table S1), and the open triangles indicate the reference event for each RE sequence, which are placed at zero (baseline). The  $2\sigma$  standard deviations in  $\delta V_S$  and  $\delta V_{LR}$  are discussed in the text. An enlarged view is displayed in the inset to better present the recovery of  $\delta V$  (open circles) during the 2005–2006 time period.

Similar discrepancies between  $\tau_S$  and  $\tau_{LR}$  are consistently detected among all of the Sumatra and Nias RE sequences at station PSI after late 2007 (Figure 4). Furthermore, some of the  $P$  coda lag times ( $\tau_P$ ) and  $\tau_S$  measurements reveal detectable seismic-velocity changes in the  $P$  wave coda and the direct  $S$  wave onset during the first week following the 2005 Nias earthquake. Note that the  $\tau(t)$  values for the S1 and S4 Sumatra RE sequences possess smaller values and fluctuate around 0 for the HF coda waves (Figures 4e and 4g). The monotonic increase in  $\tau_P$  only holds for the target events that occurred within the first week following the 2005 earthquake, with calculated  $\tau_P$  values of up to +0.03 s (thick light-blue curves in Figures 4c and 5b–5g). Because the  $\tau_P$  values are a factor of 2 smaller than the  $\tau_S$  values (e.g., Figure 3a of W. Yu et al., 2013a) to begin with, given the same decay rate, the  $\tau_P$  values largely decreased to zero after the first week following the 2005 mainshock (Figures 4a and 5a). For the target events that exhibit nonzero  $\tau_P$ , the  $\tau_S$  values at the direct  $S$  wave onset are of about +0.03 s (thick light-blue curves in Figures 4c and 5b–5g).

We use a kernel density estimation (Parzen, 1962) with adequate bandwidths to assess the overall distribution of the  $\delta V_S$  and  $\delta V_{LR}$  measurements whose time separations are longer than half a year and establish the consistency and robustness of the observed  $\delta V_S$  and  $\delta V_{LR}$  trends (Figures 3c and 3d). The kernel density estimation is a representation of the probability density function and can be formulated as follows:

$$\hat{f}_h(x) = \frac{1}{n} \sum_{i=1}^n K\left(\frac{x-x_i}{h}\right), \quad (5)$$

where  $x_i$  is the  $i$ th  $\delta V$  data of the total sample size  $n$ ,  $h$  is the bandwidth value that controls the smoothness of the resulting probability density curve, and  $K(x_i, h)$  is the kernel expressed in Gaussian function:

$$K(x_i, h) = \frac{1}{h\sqrt{2\pi}} e^{-\frac{1}{2}\left(\frac{x-x_i}{h}\right)^2}. \quad (6)$$

The peaks correspond to the maximum likelihood values for each set of  $\delta V$  data. Note that the break from the  $\delta V_{LR}$  recovery after late 2007 is likely caused by both the 2007 Bengkulu and 2008 Simeulue earthquakes (to be discussed in section 5). We adopt the timing of the 2007 earthquakes to sort the  $\delta V$  values into two groups, before (blue curve, Group 1) and across the 2007 earthquakes (red curve, Group 2); the 2007 earthquakes were simply chosen for this division since they occurred first. We observe a noticeable contrast between the Group 1 and Group 2  $\delta V$  values. The peak  $\delta V_S$  value changes from -0.04% in Group 1 to +0.007% in Group 2, indicating continuous velocity recovery (Figure 3c), whereas the peak  $\delta V_{LR}$  value changes from -0.16% in Group 1 to -0.25% in Group 2, indicating an additional velocity reduction and minimum recovery after 2007 (Figure 3d). The post-2007  $\delta V_{LR}$  values (Group 2) are typically a factor of 2 larger than those measured earlier in the time series (Group 1). The steady  $\delta V_S$  recovery at Station PSI after the 2004/2005 earthquakes is consistent among all of the Sumatra and Nias RE sequences (left panels of Figures 6 and 7). The  $\delta V_{LR}$  values consistently exhibit substantial offsets of -0.3% to -0.6% for all of the RE sequences across the late 2007 timeframe (right panels of Figures 6

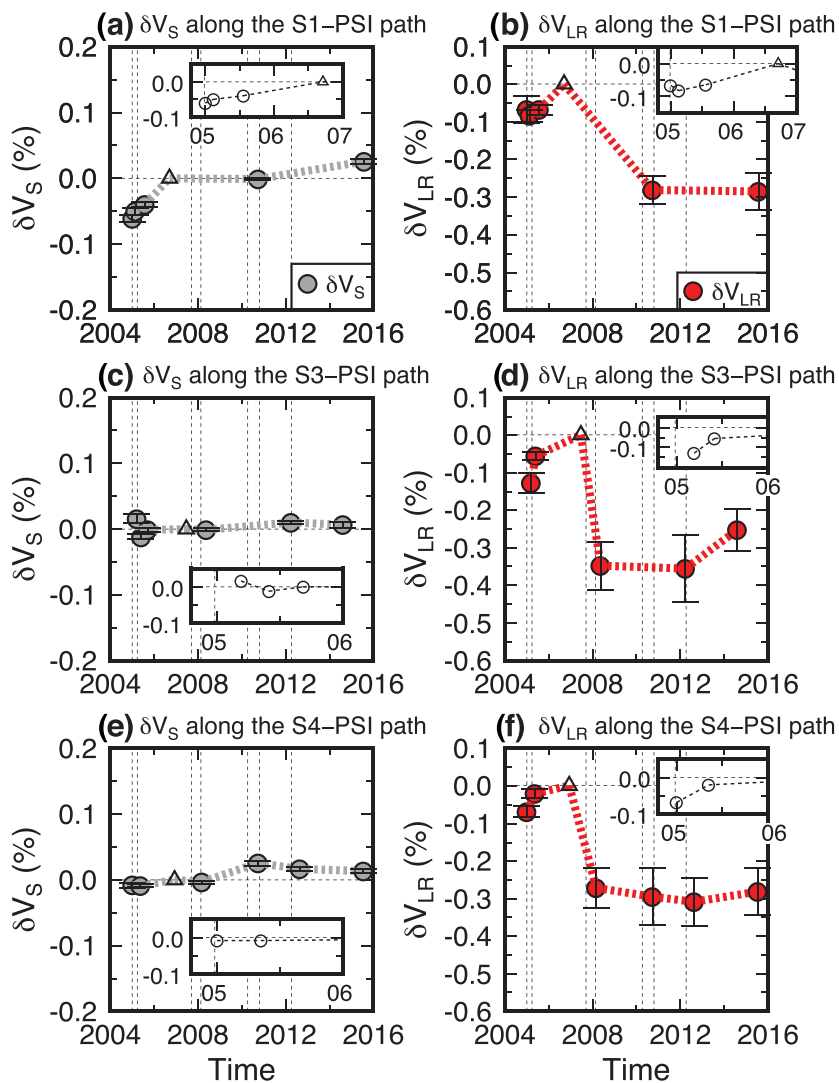


**Figure 7.** Computed  $\delta V_S$  and  $\delta V_{LR}$  for the Sumatra RE sequences recorded at station PSI: (a, b) S1, (c, d) S3, and (e, f) S4 over the 2005–2015 time period. The figure symbols are same as in Figure 6.

and 7). We conclude that this is a robust observation displaying clear bifurcation in the temporal variations of  $\delta V_{LR}$  and  $\delta V_S$ .

#### 4. Finite Difference Synthetics and $\tau(t)$ Investigation

The two-dimensional elastic finite difference (FD) method (Helmberger & Vidale, 1988; Vidale & Helmberger, 1988) is used to compute the synthetic seismograms. Our goal is to explore the seismic velocity model parameters that are sensitive to the first-order pattern of the observed  $\tau_S$  and  $\tau_{LR}$  trends. Our one-dimensional (1-D) reference velocity model, termed “mST2,” is a combination of the ST2 model (upper 50 km) (Lange et al., 2010) and isotropic Preliminary reference Earth model (PREM; 50- to 370-km depth) (Dziewonski & Anderson, 1981). The ST2 velocity model is derived from regional  $P$  and  $S$  wave traveltimes whose phases sampled the Sumatra Subduction Zone. Here we perturb the  $P$  wave velocity ( $\alpha$ ),  $S$  wave velocity ( $\beta$ ), and layer thickness of the mST2 model for our sensitivity analysis (Figures 8a and 8b). Random media are adopted for all of the models, which are defined by Gaussian correlation functions with RMS perturbations and correlation lengths in the  $x$  and  $z$  directions ( $clx$  and  $clz$ , respectively) (Frankel & Clayton, 1986). A two-dimensional (2-D) random-media reference velocity

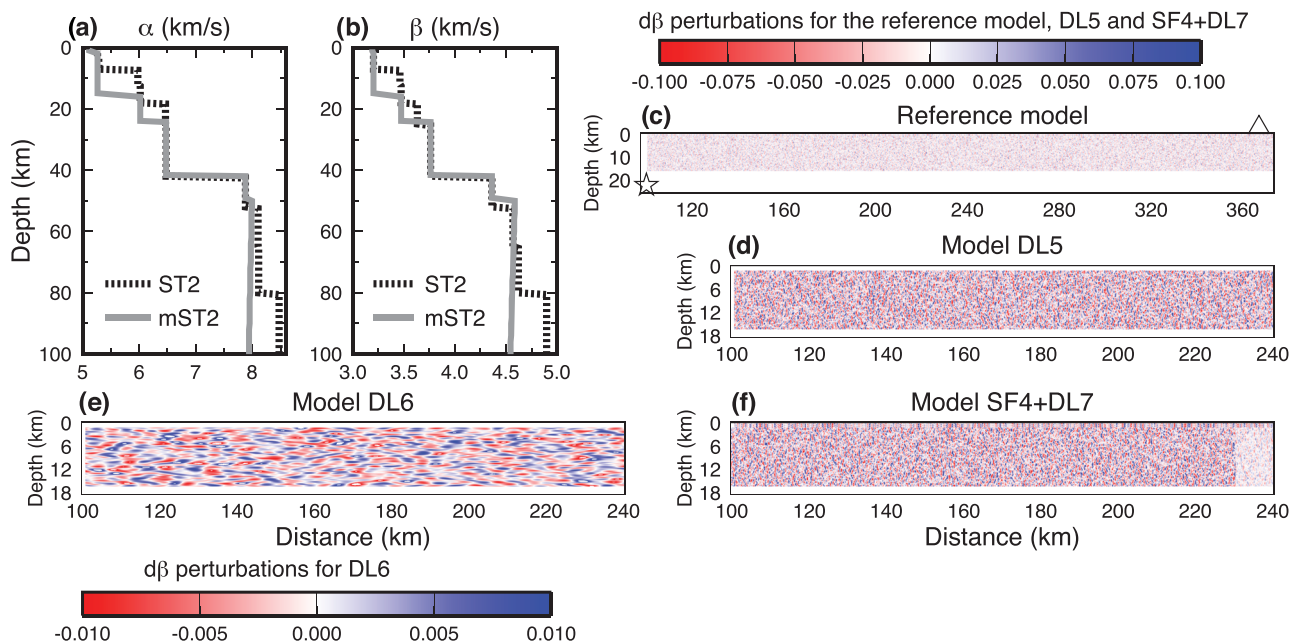


**Figure 8.** One-dimensional (a)  $P$  wave velocity ( $\alpha$ ) and (b)  $S$  wave velocity ( $\beta$ ) structures of the mST2 reference velocity model (gray line), which is modified from the ST2 (dotted black line) (Lange et al., 2010) and PREM (Dziewonski & Anderson, 1981) models; the upper 100 km of the velocity model is displayed here. (c–f) Lateral  $d\beta$  perturbations of several two-dimensional random-media models: (c) reference model, (d) DL5, (e) DL6, and (f) SF4 + DL7. The presented models are adopted for simulating wave propagation from the N1 RE sequence to station PSI. The source (star) and receiver (triangle) in (c) are positioned at (100, 22) and (367, 0), respectively, and the FD regime is displayed from  $x = 98$  to 373 km and  $z = 0$  to 25 km. The FD regime in (d)–(f) is displayed from  $x = 100$  to 240 km and  $z = 0$  to 18 km. Note that color scales for  $d\beta$  perturbations of (e) the DL6 model are different from those of (c), (d), and (f) other models. The perturbed parameters of each presented model are listed in Table 1.

model is formed from the 1-D mST2 velocity model using the following parameters: RMS = 10%,  $clx = 0.5$  km and  $clz = 0.5$  km (isotropic, with an aspect ratio  $clx/clz = 1$ ; see Table 1). We consider two end-member models, “deep layer” (DL) and “surface” (SF). The settings for the DL models include superposed background velocity  $d\alpha$  and  $d\beta$  perturbations and variations in the  $clx/clz$  aspect ratio and RMS in the upper 1–16 km of the crust, whereas the settings for the SF models include superposed  $d\beta$  perturbations,  $clx/clz$ , and RMS variations that are confined to the uppermost 0.5–1.0 km. The perturbed parameters for each model are presented in Table 1.

We consider the geometry of the N1 sequence recorded at station PSI for most of the computations, with a 22-km focal depth for the N1 RE sequence and 267-km epicentral distance from Station PSI. The dimensions of the FD regime are 500 km  $\times$  220 km ( $x$  direction  $\times$   $z$  direction), and the length of the time window is 170 s, with a 0.0625-km grid spacing and 3.125-ms time step used during the computation. The source is positioned at  $x = 100$  km and  $z = 22$  km. The random-media regime extends from  $x = 101.5$  km to  $x = 500$  km and from  $z = 0$  km to  $z = 1$  km for SF models and from  $z = 1$  km to  $z = 16$  km for DL models (Figure 8c). The FD synthetics are accurate up to 6.0 Hz. We also present two examples where we consider the geometry of the S1 sequence at Station PSI, with a 48-km focal depth for the S1 RE sequence and 534-km epicentral distance from station PSI. The dimensions of the FD regime are 900 km  $\times$  370 km ( $x$  direction  $\times$   $z$  direction) for the S1-PSI geometry, and the length of the time window is 280 s, with a 0.125-km grid spacing and 6.25-ms time step. The source is positioned at  $x = 100$  km and  $z = 48$  km. The precision of the synthetic seismograms for S1 is accurate up to 3.0 Hz.  $clz$  is fixed at 0.5 km, meaning each scatter includes four and eight grid cells in the  $z$  direction for the S1-PSI and N1-PSI regimes, respectively. We use a dip-slip focal mechanism and 1-s triangle source time function. The HF synthetic seismograms are band-pass filtered between 0.4 and 1.6 Hz. The synthetic  $\tau(t)$  values that are computed from the synthetic seismograms are based on the perturbed models relative to the reference model using a sliding-window CC approach, which is identical to the approach used to obtain the observed  $\tau(t)$  values. Note that synthetic scattered wavefields are computed with the 2-D elastic FD method, and intrinsic attenuation ( $Q$ ) is not included in the computation. The 2-D nature and lack of attenuation are probably the factors that contribute to the dissimilarity between the synthetic

**Table 1**

*List of Models Used for the Finite Difference Synthetics Computations and the Associated Parameters That Were Modified to Perturb the mST2 Reference Velocity Model*

Model ID	Parameters that were modified to perturb the mST2 reference velocity model
Reference random-media model	RMS = 10%, $clx = 0.5$ km, and $clz = 0.5$ km over the 0- to 1- and 1- to 16-km-depth ranges for the surface (SF) and deep layer (DL) models, respectively
N1 SF-LSRC1 (surface)	$d\beta = -4\%$ , RMS = 25%, $clx = 0.5$ km, and $clz = 0.5$ km over the 0- to 1-km-depth range, localized to within 25 km of the source
N1 DL-LSRC1 (deep layer)	$d\alpha = -0.06\%$ , $d\beta = -0.12\%$ , RMS = 25%, $clx = 0.5$ km, and $clz = 0.5$ km over the 1- to 16-km-depth range, localized to within 25 km of the source
N1 SF-LSTN1 (surface)	$d\beta = -4\%$ , RMS = 25%, $clx = 0.5$ km, and $clz = 0.5$ km over the 0- to 1-km-depth range, localized to within 10 km of the station
N1 SF-LSTN2 (surface)	$d\beta = -16\%$ , RMS = 25%, $clx = 0.5$ km, and $clz = 0.5$ km over the 0- to 1-km-depth range, localized to within 10 km of the station
S1 SF-LSTN1 (Surface)	Similar to N1 SF-LSTN1, but with a 48-km focal depth and 534-km epicentral distance
S1 SF-LSTN2 (surface)	Similar to N1 SF-LSTN2, but with a 48-km focal depth and 534-km epicentral distance
SF1 (surface)	RMS = 13%, $clx = 0.5$ km, and $clz = 0.5$ km over the 0- to 1-km-depth range; that is, a 3% increase in the RMS perturbation relative to the reference random-media model
SF2 (surface)	RMS = 10%, $clx = 5$ km, and $clz = 0.5$ km over the 0- to 1-km-depth range; that is, a tenfold increase in the $clx/clz$ aspect ratio relative to the reference random-media model
SF3 (surface)	$d\beta = -4\%$ , RMS = 10%, $clx = 0.5$ km, and $clz = 0.5$ km over the 0- to 1-km-depth range; that is, an additional $d\beta$ perturbation relative to the reference model
SF4 (surface)	$d\beta = -4\%$ , RMS = 25%, $clx = 0.5$ km, and $clz = 0.5$ km over the 0- to 1-km-depth range
SF5 (surface)	$d\beta = -16\%$ , RMS = 10%, $clx = 0.5$ km, and $clz = 0.5$ km over the 0- to 0.5-km-depth range
SF6 (surface)	$d\beta = -16\%$ , RMS = 10%, $clx = 0.5$ km, and $clz = 0.5$ km over the 0- to 1-km-depth range
DL1 (deep layer)	RMS = 13%, $clx = 0.5$ km, and $clz = 0.5$ km over the 1- to 16-km-depth range; that is, a 3% increase in the RMS perturbation relative to the reference random-media model
DL2 (deep layer)	RMS = 10%, $clx = 5$ km, and $clz = 0.5$ km over the 1- to 16-km-depth range; that is, a tenfold increase in the $clx/clz$ aspect ratio relative to the reference random-media model
DL3 (deep layer)	$d\alpha = -0.06\%$ , $d\beta = -0.12\%$ , RMS = 10%, $clx = 0.5$ km, and $clz = 0.5$ km over the 1- to 16-km-depth range; that is, additional $d\alpha$ and $d\beta$ perturbations relative to the reference random-media model
DL4 (deep layer)	Combination of the DL1, DL2, and DL3 models
DL5 (deep layer)	$d\alpha = -0.06\%$ , $d\beta = -0.12\%$ , RMS = 25%, $clx = 0.5$ km, and $clz = 0.5$ km over the 1- to 16-km-depth range
DL6 (deep layer)	$d\alpha = -0.06\%$ , $d\beta = -0.12\%$ , RMS = 25%, $clx = 5$ km, and $clz = 0.5$ km over the 1- to 16-km-depth range
DL7 (deep layer)	$d\alpha = -0.06\%$ , $d\beta = -0.12\%$ , RMS = 25%, $clx = 0.5$ km, and $clz = 0.5$ km over the 1- to 16-km-depth range that is within 130 km of the source
SF4 + DL5	Combination of the SF4 and DL5 models
SF4 + DL6	Combination of the SF4 and DL6 models
SF4 + DL7	Combination of the SF4 and DL7 models

and observed coda waves and oscillating synthetic  $\tau(t)$  in the later part of the codas. We focus on characterizing the behaviors of the HF synthetic  $\tau_S(t)$  bounded by the vertical dotted lines in Figures 9–12.

The heterogeneous regions that can produce the observed time-dependent time delay include a localized velocity reduction near either the source or station and a velocity reduction in the bulk of the upper crust. We first examine the effect of a localized velocity reduction near either the source or station. The N1 DL-LSRC1 model produces  $\tau_P$  values of up to +0.05 s and null  $\tau_S$  values for a localized velocity reduction near the source (orange curve in Figure 9a), whereas the N1 SF-LSRC1 model produces null  $\tau_P$  and  $\tau_S$  values (light-blue curve in Figure 9a). The N1 SF-LSTN1 model produces null  $\tau_P$  and  $\tau_S$  values for a localized velocity reduction near the station (thick green curve in Figure 9a), and the S1 SF-LSTN1 model produces oscillating  $\tau_P$  and  $\tau_S$  values between –0.05 s and +0.05 s for the S1-PSI path (thick green curve in Figure 10a). Amplifying the localized S wave velocity reduction near the station from  $d\beta = -4\%$  to –16% produces a linear increase in  $\tau_S(t)$  values, with increases of +0.075 s (N1 SF-LSTN2; thick yellow curve in Figure 9a) and +0.15 s (S1 SF-LSTN2; thick yellow curve in Figure 10a), respectively, for the N1 and S1 sequences recorded by station PSI. Two lines of argument suggest that the observed  $\tau(t)$  values of the HF S coda waves are not caused by a localized near-surface velocity reduction at station PSI. (1) The perturbed models with localized velocity perturbations near the station produce a linear increase in  $\tau_S$  values, even at different distance ranges, whereas the observed  $\tau_S$  values for the S1 sequence at station PSI does not exhibit an increase in  $\tau_S(t)$  (light-blue curve in Figure 4e). (2) A monotonic increase in  $\tau_P$  values is detectable for the target

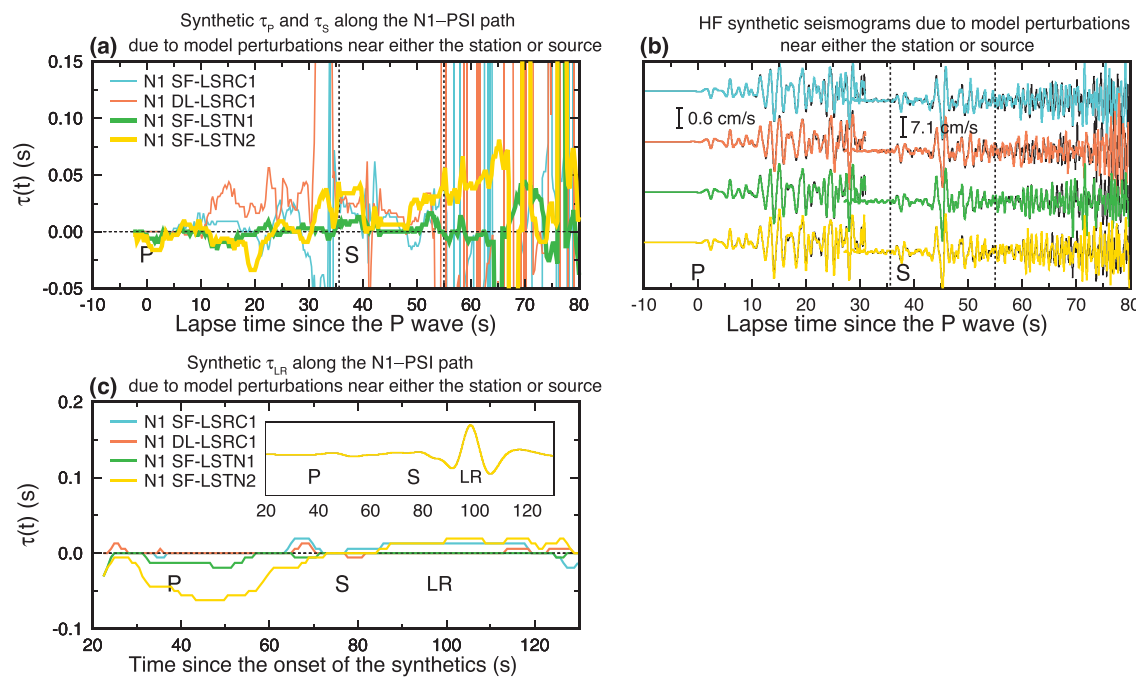


**Figure 9.** (a) Synthetic  $\tau(t)$  that were calculated from (b) the HF (0.4–1.6 Hz) FD synthetic seismograms of the N1 sequence recorded at Station PSI using models with localized velocity perturbations near either the source or Station PSI. The computed synthetic seismograms that are based on the reference model are indicated by the black traces, whereas the computed synthetic seismograms that are based on the perturbed models are indicated by the colored traces and superimposed on the reference synthetic seismograms. The  $P$  and  $S$  coda time windows are plotted separately to highlight the  $P$  codas due to their relatively low amplitudes. The amplitude scales for both the  $P$  and  $S$  waves are displayed. (c) LP (0.03–0.1 Hz) synthetic  $\tau_{LR}$  based on the same perturbed models, with the synthetic seismograms based on the reference model (black) and model N1 SF-LSTN2 (yellow) displayed in the inset. Synthetic HF  $\tau_p(t)$  and  $\tau_s(t)$  and seismograms are aligned relative to the HF  $P$  wave onset, whereas LP  $\tau_{LR}(t)$  and Rayleigh waves are aligned relative to the onset of the synthetics. The perturbed parameters of each presented model are listed in Table 1.

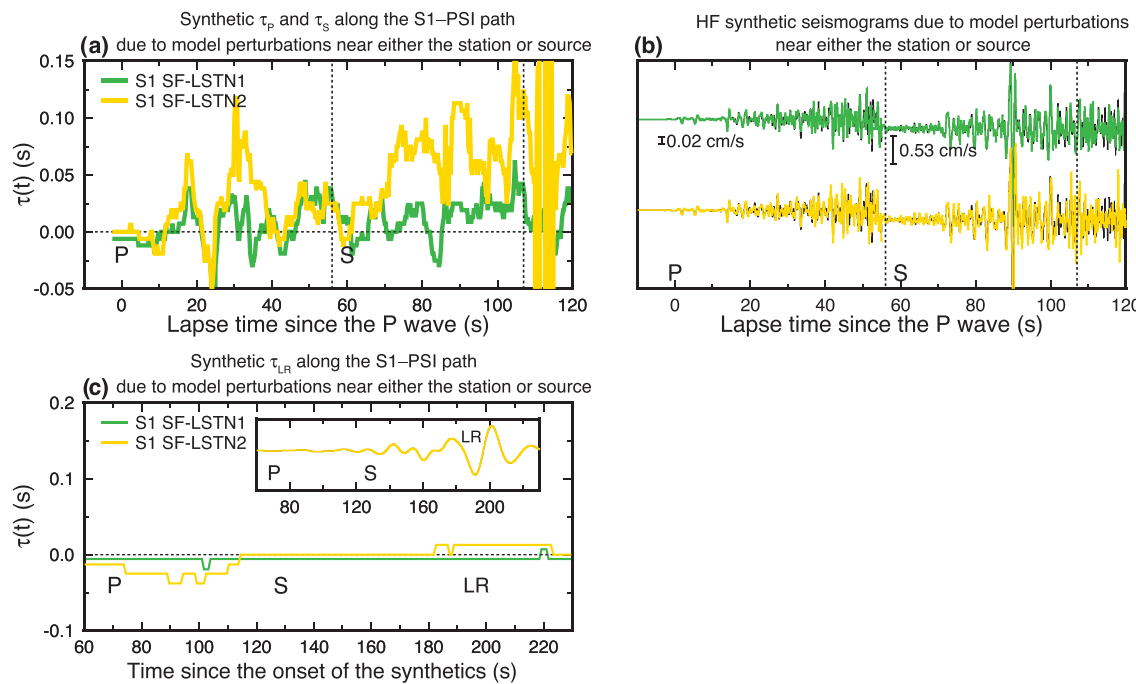


**Figure 10.** FD synthetic seismograms and corresponding  $\tau(t)$  of the S1 sequence at station PSI based on two models with a localized velocity perturbation near Station PSI. The perturbed parameters of each presented model are listed in Table 1. This figure is similar to Figure 9.

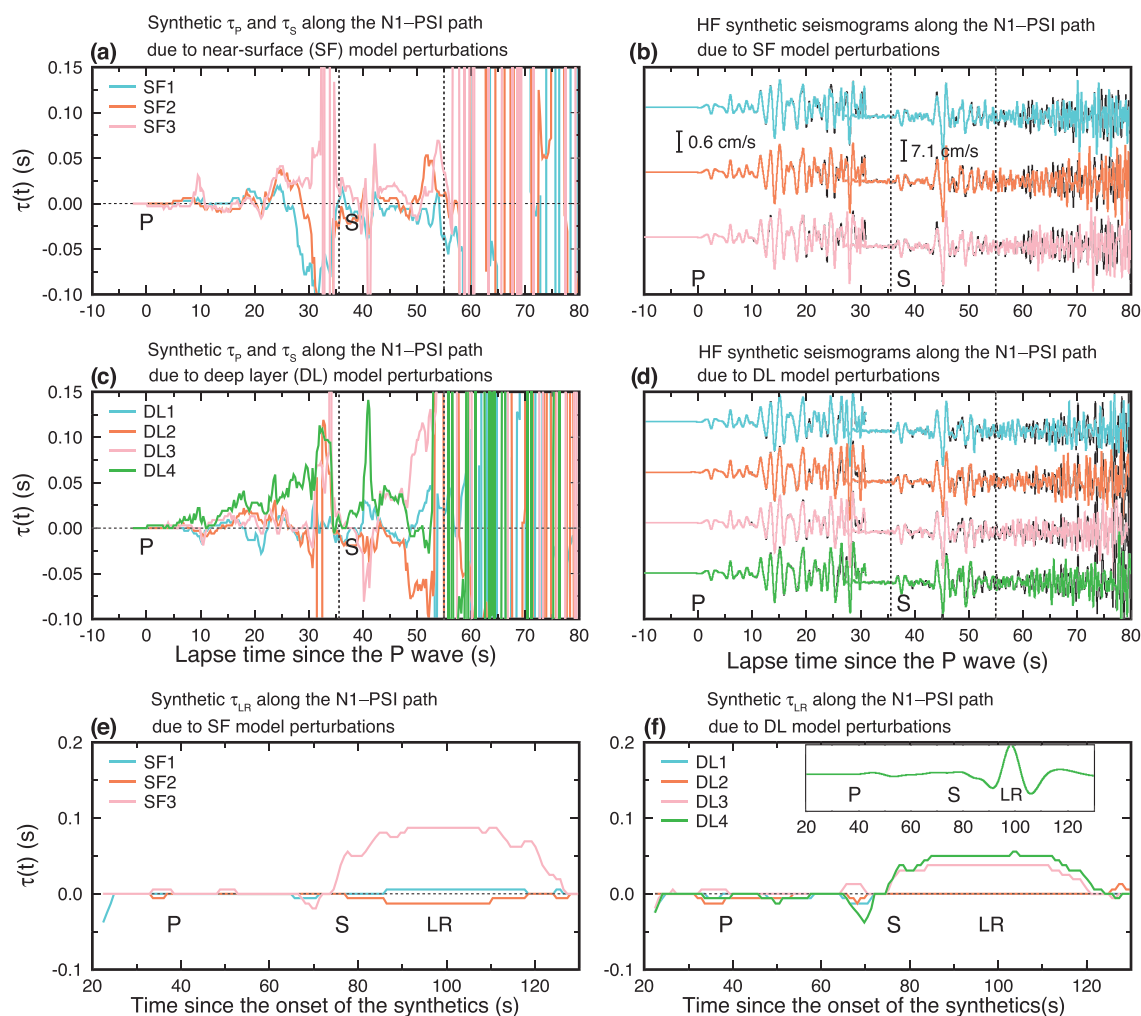


**Figure 11.** HF FD synthetic seismograms and corresponding  $\tau(t)$  using several velocity models: (a, b) “surface” (uppermost 1.0 km, denoted as “SF”) and (c, d) “deep layer” (1- to 16-km depth, denoted as “DL”) with various RMS, correlation length,  $d\alpha$ , and  $d\beta$  perturbations in the random media. Synthetic LP  $\tau_{LR}$  based on various (e) SF and (f) DL model perturbations. The LP synthetics in (f) that are computed based on the reference model and model DL4 are indicated by black and green traces, respectively. The perturbed parameters of each presented model are listed in Table 1. This figure is similar to Figure 9.

events that occurred within the first week following the Nias mainshock (Figures 4c and 5b–5g), but the smaller  $\tau_p$  values largely diminished to 0 after the first week following the Nias earthquake. The observed  $\tau_p$  and  $\tau_s$  values suggest that the velocity reduction occurs in the bulk part of the upper crust. Moreover, the localized velocity reduction near either the source or station produces  $\tau_{LR}$  values of  $< +0.03$  s (Figures 9c and 10c).

Here we discuss how the velocity reduction parameters, RMS perturbations, and  $clx/clz$  aspect ratio for the SF and DL models influence the synthetic  $\tau(t)$  values for the HF S coda and Rayleigh waves. The following FD synthetics computations employ the N1-PSI source-receiver geometry. Figure 11 displays the synthetic test results where an individual parameter is moderately perturbed, such that the sensitivity of each perturbed parameter can be assessed. Models SF1, SF2, and SF3 have a 3% RMS amplification, increase in the  $clx/clz$  ratio from 1 to 10, and additional  $d\beta = -4\%$  perturbation relative to the reference model, respectively. The synthetic  $\tau(t)$  values for the HF S coda waves that propagated through these models all exhibit subtle fluctuations around 0, with episodic oscillations at 10, 20–30, and 47–52 s (Figure 11a). Models DL1, DL2, and DL3 have a 3% RMS amplification, increase in the  $clx/clz$  aspect ratio from one to ten, and additional  $d\alpha = -0.06\%$  and  $d\beta = -0.12\%$  perturbations relative to the reference model, respectively. The 3% RMS amplification also produces subtle fluctuations in the  $\tau_p$  and  $\tau_s$  values (DL1, light-blue curve in

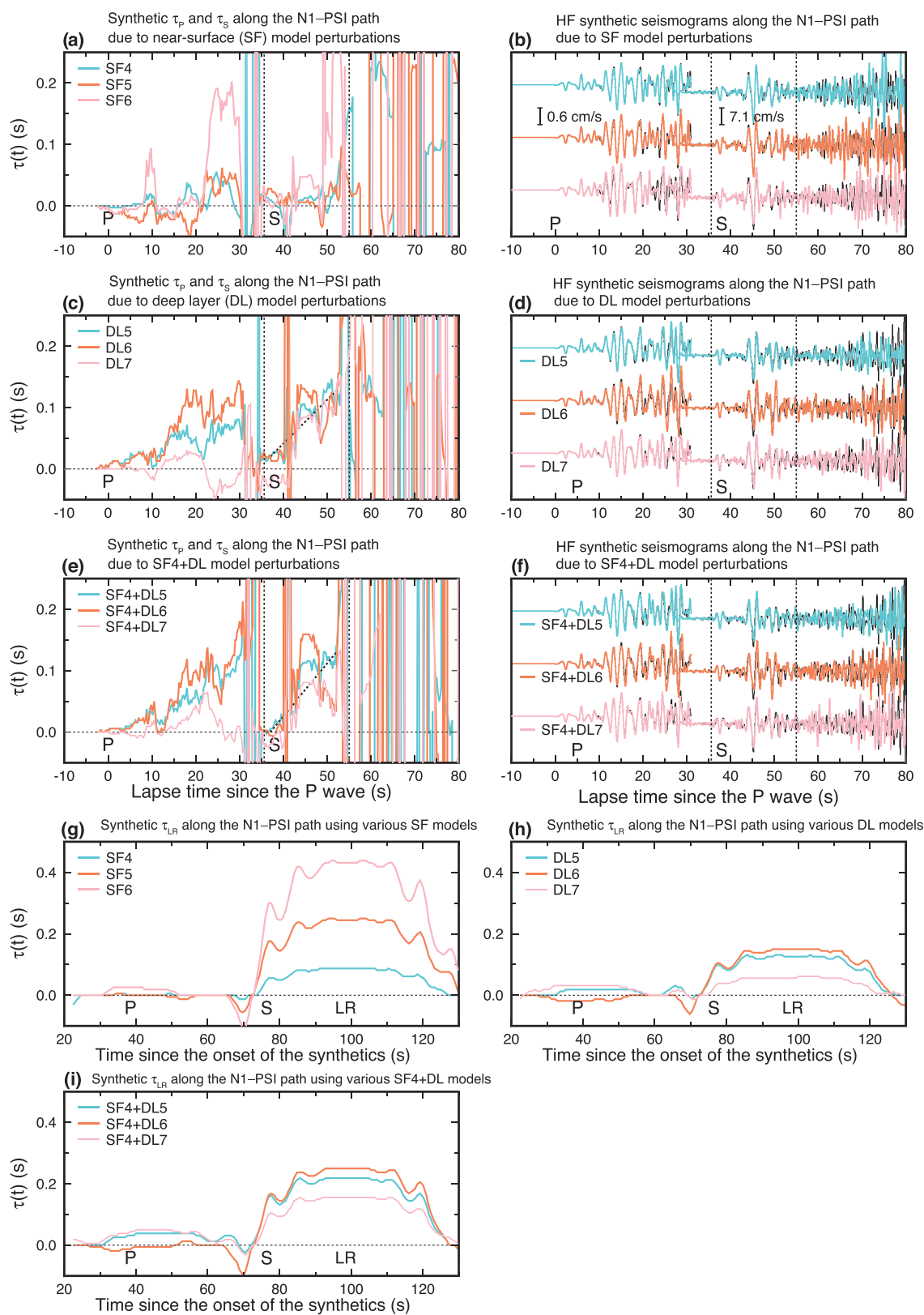


**Figure 12.** FD synthetic seismograms and corresponding  $\tau(t)$  for additional (a, b, and g) SF, (c, d, and h) DL, and (e, f, and i) SF4 + DL models. The slope of synthetic  $\tau_S(t)$  based on Models DL5 and SF4 + DL5 are equivalent to  $\delta V_S = -0.72\%$  and  $-0.86\%$ , respectively (slope indicated as dotted line in c and e). The perturbed parameters of each presented model are listed in Table 1. This figure is similar to Figure 11.

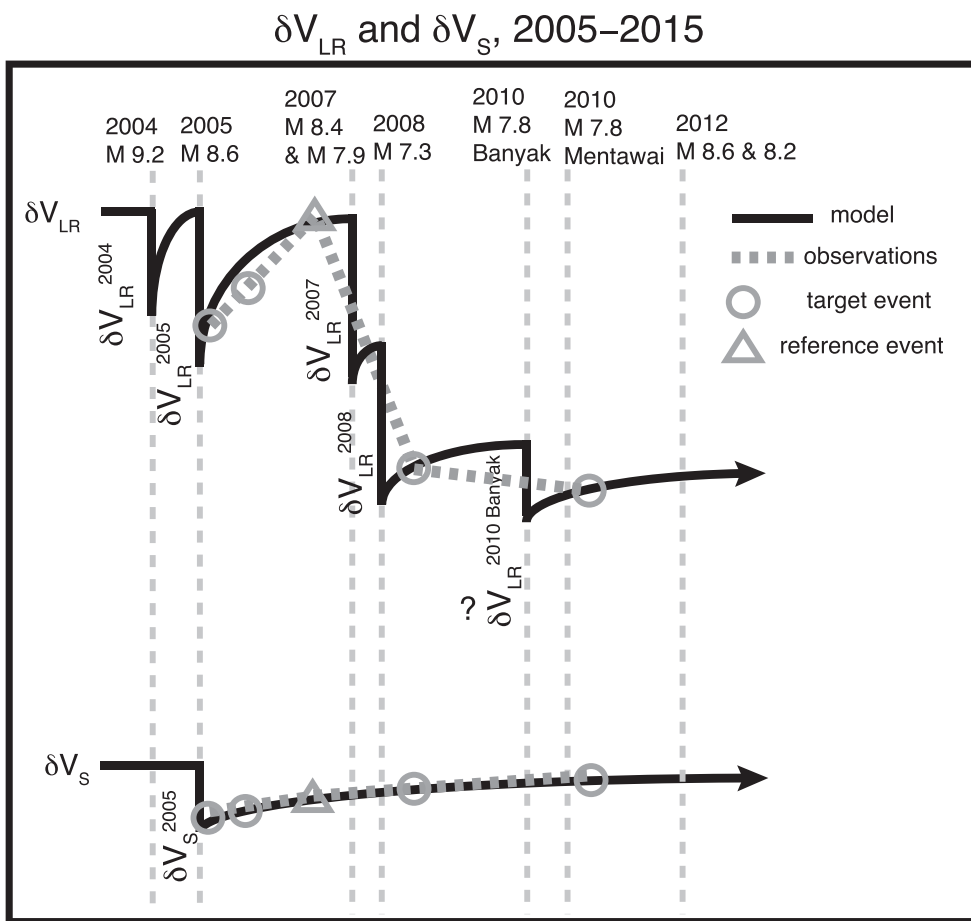


**Figure 13.** Interpretation of the observed temporal changes in  $\delta V_{LR}$  and  $\delta V_S$  induced by the 2004, 2005, 2007, 2008, 2010, and 2012 earthquakes along the Banda Aceh-Nias-Simeulue segment of the Sumatra Subduction Zone.  $\delta V_{LR}$  recovery occurs until it is interrupted by the 2007 and 2008 events. A question mark is placed next to the drop associated with the 2010 Banyak earthquake to reflect undersampling. The observations indicate an apparent static offset in  $\delta V_{LR}$  without recovery after the 2007 and 2008 events (dashed dark-gray lines).  $\delta V_S$  is reduced by the 2005 event and undergoes steady recovery during the 2005–2015 time period, in contrast to the complex time-varying  $\delta V_{LR}$  behavior.

Figure 11c). However, increasing the  $clx/clz$  aspect ratio from one to ten produces a negative  $\tau_S$  value of  $-0.07$  s at  $\sim 50$  s (DL2, orange curve in Figure 11c), and the  $d\alpha = -0.06\%$  and  $d\beta = -0.12\%$  perturbations produce an increase in the  $\tau_S$  value of up to  $+0.13$  s (DL3, pink curve in Figure 11c). Model DL4, which includes all of the perturbations in models DL1, DL2, and DL3, produces a monotonic increase in  $\tau_P$ , as well as smaller  $\tau_S$  values at  $\sim 50$  s (green curve in Figure 11c). The smaller  $\tau_S$  values mimic the negative  $\tau_S$  values in the DL2 model at 47–52 s due to the increase in the  $clx/clz$  aspect ratio.

We now consider the effects of RMS amplification and perturbing several parameters within a given velocity model. A monotonic increase in both  $\tau_P(t)$  and  $\tau_S(t)$  is still better approximated by the DL models for the HF P and S wave codas (DL5 and DL6 in Figure 12c). The SF models with a strong S wave velocity reduction ( $d\beta = -16\%$ ) produce oscillating  $\tau_P(t)$  and  $\tau_S(t)$  values with peaks at 10, 20–30, and 47–52 s (SF5 and SF6 in Figure 12a). The DL models with RMS = 25%,  $d\alpha = -0.06\%$ ,  $d\beta = -0.12\%$  perturbations, and  $clx/clz = 1$  produces linear increases of up to  $+0.072$  and  $+0.147$  s in  $\tau_P$  and  $\tau_S$ , respectively (DL5, light-blue curve in Figure 12c; the 2D  $d\beta$  profile is displayed in Figure 8d). The  $\tau_P$  values increase by a factor of 1.5 when the  $clx/clz$  aspect ratio is increased to 10, with a value of up to  $0.11$  s; the  $\tau_S$  values are larger up to  $+0.138$  s over the 40- to 45-s window, but then decrease over the 47- to 52-s window (DL6, orange curve in Figure 12c; the 2-D  $d\beta$  profile is displayed in Figure 8e). This  $\tau_S$  pattern of an increase followed by a drop over the 47- to 52-s window is similar to that observed for models DL3 and DL4 (Figure 11c). The heterogeneous region in model

DL7 only spans 50% of that in model DL5; its predicted  $\tau_P$  values exhibit an increase over the 10- to 20-s window to +0.025 s, followed by a drop over the 20- to 30-s window to -0.03 s, whereas the  $\tau_S$  values exhibit a monotonic increase up to +0.1 s (DL7, pink curve in Figure 12c). The combined perturbations of the SF and DL models produce  $\tau_P$  and  $\tau_S$  values that are similar to those based calculated from the DL models, with larger  $\tau_P$  and smaller  $\tau_S$  values often obtained (Figure 12e; the 2-D  $d\beta$  profile of model SF4 + DL7 is displayed in Figure 8f). The slope of synthetic  $\tau_S(t)$  based on the above DL and combined perturbations of the SF and DL models estimate  $\delta V_S$  in the range of -0.61% (DL6) and -0.98% (DL7), slightly lower than the observed  $\delta V_S$  immediately after the 2005 event (Figures 3 and 6). Models DL5 and SF4 + DL5 produce  $\delta V_S = -0.72\%$  and -0.86%, respectively, indicated as the slope of dotted line in Figures 12c and 12e.

LP Rayleigh waves are sensitive to  $d\beta$  reductions and RMS amplification in the bulk crust, with models SF3, SF4, DL3, and DL4 producing  $\tau_{LR}$  values of +0.087, +0.087, +0.038, and +0.05 s, respectively (Figures 11e, 11f, and 12g). Models SF5 and SF6 produce  $\tau_{LR}$  values in the +0.244- to +0.431-s range (Figure 12g). Models DL5–DL7 have fixed RMS = 25%,  $d\alpha = -0.06\%$ , and  $d\beta = -0.12\%$  perturbation; an increase in the  $clx/clz$  aspect ratio from 1 to 10 produces an increase in  $\tau_{LR}$  from +0.125 s (DL5) to +0.150 s (DL6), whereas a reduction in the heterogeneous region in model DL7 produces a maximum  $\tau_{LR}$  value of only +0.056 s (Figure 12h). Combinations of the SF4 model and various DL models have also been used to produce synthetic  $\tau_{LR}$  values, with  $\tau_{LR}$  values of +0.219, +0.250, and +0.156 s obtained for models SF4 + DL5, SF4 + DL6, and SF4 + DL7, respectively (Figure 12i).

Our modeling results indicate that a strong *S* wave velocity reduction in the near surface substantially contributes to the large  $\tau_{LR}$  values but has a minimal effect on the observed  $\tau_P$  and  $\tau_S$  patterns. A subtle *S* wave velocity reduction in the upper crust is necessary to account for the observed  $\tau_P$  and  $\tau_S$  patterns and can also partially contribute to the  $\tau_{LR}$  pattern. Depending on the availability of early  $\tau_S$  and  $\tau_{LR}$  measurements after the 2004/2005 mainshocks, the amount of the *S* wave velocity reduction in the near surface and upper crust can be scaled accordingly. Our preferred explanation is as follows. The observed  $\tau_S$  and  $\tau_{LR}$  patterns after the 2004/2005 earthquakes may reflect the combination of a strong *S* wave velocity reduction in the near surface and a subtle *S* wave velocity reduction in the upper crust. However, the  $\tau_{LR}$  amplification and the null  $\tau_S$  after late 2007 predominantly reflects another substantial *S* wave velocity reduction in the near surface (red curves in Figure 4). The scattering media changing from isotropic ( $clx/clz = 1$ ) to vertically transverse isotropic ( $clx/clz = 10$ ) and amplifying the RMS can influence *S* coda and Rayleigh wave propagation, thereby altering the  $\tau_S$  and  $\tau_{LR}$  values. We discuss the likely scenarios that can potentially explain these observations and modeling results in the following section.

## 5. Discussion and Conclusions

### 5.1. $\delta V_S$ Recovery After the 2004 and 2005 Earthquakes

Obermann et al. (2013) positioned the source and receiver at the surface in their coda wave computations and suggested that the later part of the coda waves were predominantly sensitive to the bulk velocity heterogeneities of the media, with the sensitivity of these waves to the source depth being approximately bounded by the length scale of the mean free path. Here we position the source and receiver at 22-km depth and the surface, respectively, in our FD simulations. Our FD synthetic tests reveal that the DL models with subtle *S* wave velocity perturbations that are confined to the upper 1–16 km produce characteristics that are consistent with a monotonic increase in  $\tau_S$  (Figure 12c), whereas the SF models with near-surface velocity perturbations (confined to the uppermost 0.5–1.0 km) cannot reproduce this key feature (Figure 12a). Although the source-receiver geometries of the two modeling approaches are different, our inferences on the sensitivity of the later part of the coda waves to the bulk heterogeneities of the media are consistent with those in Obermann et al. (2013).

The  $\delta V_S$  observations show continuous recovery from 2005 to 2015. It is unlikely that the  $\delta V_S$  induced by coseismic slip would be sustained for several years, even though the deformation induced by large earthquake coseismic slip can produce structural changes in the bulk crust and time-varying  $\delta V_S$  behavior. Additional independent arguments suggest that the continuous  $\delta V_S$  recovery from 2005 to 2015 was predominantly controlled by deep postseismic afterslip or/and viscoelastic relaxation processes. The REs associated with the 2004 and 2005 earthquakes are located close to the afterslip zones, at depths of about 50

and 25 km, respectively (Figure 1 and Table S2). The postseismic displacement time series recorded by GPS Stations UMLH and LEWK, and the GPS normalized displacement time series relative to the concurrent  $\delta V_S$  values are provided in Figures S4 and S5, respectively, for comparison. Note that the details of the GPS data processing can be found in Feng et al. (2015). The logarithmic recovery of  $\delta V_S$  corresponds to the postseismic deformation time series reasonably well. Feng et al. (2015) suggested that viscoelastic relaxation was essential for explaining the long-term geodetic measurements. Qiu et al. (2018) recently estimated a background upper mantle viscosity of  $10^{17}$ – $10^{19}$  Pa s beneath the Sumatra region, which would indicate relaxation timescales (days to years) that are similar to our observed timescales of  $\delta V_S$  recovery.

### 5.2. Multiple $\delta V_{LR}$ Reductions Induced by the 2004, 2005, 2007, and 2008 Earthquakes

The observed  $\delta V_{LR}$  values at Station PSI from late 2007 to early 2008 exhibit a remarkable reduction of at least  $-0.3\%$ , which is a factor of 2 larger than the reductions caused by the 2004 and 2005 earthquakes (Figures 3, 6, and 7). These new data reveal that the  $\delta V_{LR}$  reduction after the 2004, 2005, 2007, and 2008 earthquakes progressively increases; that is,  $\delta V_{LR}^{2007/2008} > \delta V_{LR}^{2005} > \delta V_{LR}^{2004}$ . Note that substantial  $\delta V_{LR}$  reductions are likely caused by the 2007  $M_w$  8.4 and  $M_w$  7.9 and 2008  $M_w$  7.3 earthquakes. It is difficult to assess the temporal resolution of  $\delta V_{LR}$  using the RE sequences due to the undersampling during the 5-month period when the 2007 and 2008 earthquakes occurred. Previous studies have suggested that earthquake-induced velocity reduction is often associated with high PGV (Hobiger et al., 2016; Rubinstein & Beroza, 2004b). We examine the PGV of the large earthquakes recorded by Station PSI in the 0.5- to 2.0-Hz frequency band (Table S3). The PGV amplitude of the 2005  $M_w$  8.6 earthquake is larger than that of the 2004  $M_w$  9.2 event, and the PGV amplitudes of the 2007  $M_w$  8.4 and  $M_w$  7.9, and 2008  $M_w$  7.3 earthquakes are smaller than those of the 2005  $M_w$  8.6 event, even though a stronger  $\delta V_{LR}$  reduction that is associated with the 2007 and 2008 earthquakes is detected. We speculate that the strong GM induced by the 2004 and 2005 events made the subsurface cracks and fractures more susceptible to the GM induced by the 2007 and 2008 earthquakes, resulting in another substantial velocity reduction.

### 5.3. Temporal Changes in $\delta V$ During 2005–2015

REs discretely sample  $\delta V$  with a limited temporal resolution. However, concurrent  $\delta V_S$  and  $\delta V_{LR}$  observations, and the differences in their temporal patterns offer new insights into the diverse processes that modulate media properties. Figure 13 summarizes the decadal  $\delta V_S$  and  $\delta V_{LR}$  observations and illustrates our inferences on the evolution of the crustal seismic-velocity structure along the Banda Aceh-Nias-Simeulue segment of the Sumatra Subduction Zone. A subtle  $-0.1\%$   $\delta V_S$  reduction due to the 2004 and/or 2005 earthquakes is followed by steady recovery, with no noticeable disruption from 2005 to 2015 ( $\delta V_S$  in Figure 13). However, a  $-0.1\%$   $\delta V_{LR}$  reduction is induced by the 2004 earthquake, and a slightly larger  $-0.1$  to  $-0.3\%$  reduction is induced by the 2005 event. We find that  $\delta V_{LR}$  experiences recovery until late 2007, with the GM from the 2007 and 2008 earthquakes then inducing a substantial  $\delta V_{LR}$  reduction ( $-0.3\%$  to  $-0.6\%$ ) that possibly occurred in multiple steps. We speculate that any  $\delta V_{LR}$  caused by the 2010 Banyak earthquake may have gone undetected due to the limited temporal resolution of the data, resulting in the observed gentle velocity recovery trend.

In summary, the differences in the temporal evolution of  $\delta V_S$  and  $\delta V_{LR}$  inferred from REs are a powerful tool for discriminating between the mechanisms that drive seismic-velocity changes after great earthquakes. Steady  $\delta V_S$  recovery is consistent with the logarithmic time dependence inferred from postseismic GPS data (Figures S4 and S5), which predominantly reflects afterslip that occurred in the updip and downdip sections of the rupture area (Feng et al., 2015) (Figure 1) and/or viscoelastic relaxation after the 2004 and 2005 earthquakes. Furthermore, two-dimensional FD synthetics computations demonstrate that the monotonic increase in the observed  $\tau_S$  values can be explained by a subtle velocity reduction of  $d\beta = -0.12\%$  at 1- to 16-km depth (DL5 in Figure 12c). However,  $\delta V_{LR}$  displays additional drops after the large earthquakes during the 2007–2008 time period, breaking the pattern of monotonic recovery. The model with a subtle S wave velocity reduction at 1- to 16-km depth can partly account for the observed  $\tau_{LR}$  pattern after the 2004/2005 events, but it is insufficient to produce values that are comparable to the observed  $\tau_{LR}$  pattern after late 2007. Strong S wave velocity reductions of  $d\beta = -4\%$  and  $-16\%$  that are confined to the uppermost 0.5–1.0 km can generally account for the observed  $\tau_{LR}$  values after 2005 and late 2007, respectively (Figure 12g). These

sudden changes are primarily associated with a cycle of damage, healing, and redamage in the subsurface layer (Sawazaki et al., 2015, 2018; Vidale & Li, 2003).

## Data Availability Statement

The seismic data analyzed in this paper were assembled from the PS network, which were downloaded from the JAMSTEC data center, Japan (<http://p21.jamstec.go.jp/top/>; last accessed on 23 August 2019).

## Acknowledgments

W. Y. wishes to thank Lujia Feng of the Earth Observatory of Singapore (EOS), Nanyang Technological University (NTU), for providing the processed GPS displacement time series presented in the study, and Louisa L. H. Tsang of EOS, NTU, for providing the slip model for the 2007 Bengkulu earthquake. We thank Kathryn Materna and an anonymous reviewer for constructive reviews. W. Y. also wishes to thank Haekal A. Haridhi, Chi-Hsien Tang, and Bor-Shou Huang of Academia Sinica, Chun-Hsiang Kuo of the National Center for Research on Earthquake Engineering, and Shengji Wei of EOS, NTU, for insightful discussions. This study was supported by the Institute of Earth Sciences, Academia Sinica and Grants MOST-104-2116-M-001-010-, MOST-106-2116-M-001-009-, and MOST-107-2116-M-001-014- from the Ministry of Science and Technology, Taiwan, Republic of China. T. R. A. S. acknowledges support from the Natural Environment Research Council (NE/P001378/1 and NE/T001372/1), UK.

## References

- Ammon, C. J., Ji, C., Thio, H. K., Robinson, D., Ni, S. D., Hjorleifsdottir, V., et al. (2005). Rupture process of the 2004 Sumatra–Andaman earthquake. *Science*, 308(5725), 1133–1139. <https://doi.org/10.1126/science.1112260>
- Barbot, S., & Fialko, Y. (2010). A unified continuum representation of post-seismic relaxation mechanisms: Semi-analytic models of afterslip, poroelastic rebound and viscoelastic flow. *Geophysical Journal International*, 182(3), 1124–1140. <https://doi.org/10.1111/j.1365-246X.2010.04678.x>
- Bird, P. (2003). An updated digital model of plate boundaries. *Geochemistry, Geophysics, Geosystems*, 4(3), 1027. <https://doi.org/10.1029/2001GC000252>
- Brenguier, F., Campillo, M., Hadzioannou, C., Shapiro, N. M., Nadeau, R. M., & Larose, E. (2008). Postseismic relaxation along the San Andreas fault at Parkfield from continuous seismological observations. *Science*, 321(5895), 1478–1481. <https://doi.org/10.1126/science.1160943>
- Chlieh, M., Avouac, J. P., Hjorleifsdottir, V., Song, T. R. A., Ji, C., Sieh, K., et al. (2007). Coseismic slip and afterslip of the great Mw 9.15 Sumatra–Andaman earthquake of 2004. *Bulletin of the Seismological Society of America*, 97(1A), S152–S173. <https://doi.org/10.1785/0120050631>
- Dziewonski, A. M., & Anderson, D. L. (1981). Preliminary reference Earth Model. *Physics of the Earth and Planetary Interiors*, 25(4), 297–356. [https://doi.org/10.1016/0031-9201\(81\)90046-7](https://doi.org/10.1016/0031-9201(81)90046-7)
- Feng, L. J., Hill, E. M., Banerjee, P., Hermawan, I., Tsang, L. L. H., Natawidjaja, D. H., et al. (2015). A unified GPS-based earthquake catalog for the Sumatran plate boundary between 2002 and 2013. *Journal of Geophysical Research: Solid Earth*, 120, 3566–3598. <https://doi.org/10.1002/2014JB011661>
- Fialko, Y. (2004). Evidence of fluid-filled upper crust from observations of postseismic deformation due to the 1992 Mw7.3 Landers earthquake. *Journal of Geophysical Research*, 109, B08401. <https://doi.org/10.1029/2004JB002985>
- Fielding, E. J., Lundgren, P. R., Bürgmann, R., & Funning, G. J. (2009). Shallow fault-zone dilatancy recovery after the 2003 Bam earthquake in Iran. *Nature*, 458(7234), 64–68. <https://doi.org/10.1038/nature07817>
- Frankel, A., & Clayton, R. W. (1986). Finite-difference simulations of seismic scattering: Implications for the propagation of short-period seismic waves in the crust and models of crustal heterogeneity. *Journal of Geophysical Research*, 91(B6), 6465–6489. <https://doi.org/10.1029/JB091iB06p06465>
- Froment, B., Campillo, M., Chen, J. H., & Liu, Q. Y. (2013). Deformation at depth associated with the 12 May 2008 MW 7.9 Wenchuan earthquake from seismic ambient noise monitoring. *Geophysical Research Letters*, 40, 78–82. <https://doi.org/10.1029/2012GL053995>
- Gudmundsson, Ó., & Sambridge, M. (1998). A regionalized upper mantle (RUM) seismic model. *Journal of Geophysical Research*, 103(B4), 7121–7136. <https://doi.org/10.1029/97JB02488>
- Helmberger, D. V., & Vidale, J. E. (1988). Modeling strong motions produced by earthquakes with two-dimensional numerical codes. *Bulletin of the Seismological Society of America*, 78(1), 109–121.
- Hill, E. M., Yue, H., Barbot, S., Lay, T., Tapponnier, P., Hermawan, I., et al. (2015). The 2012 Mw 8.6 Wharton Basin sequence: A cascade of great earthquakes generated by near-orthogonal, young, oceanic mantle faults. *Journal of Geophysical Research: Solid Earth*, 120, 3723–3747. <https://doi.org/10.1002/2014JB011703>
- Hobiger, M., Wegler, U., Shiomi, K., & Nakahara, H. (2016). Coseismic and post-seismic velocity changes detected by Passive Image Interferometry: Comparison of one great and five strong earthquakes in Japan. *Geophysical Journal International*, 205(2), 1053–1073. <https://doi.org/10.1093/gji/ggw066>
- Hoehner, A., Sobolev, S. V., Einarsson, I., & Wang, R. J. (2011). Investigation on afterslip and steady state and transient rheology based on postseismic deformation and geoid change caused by the Sumatra 2004 earthquake. *Geochemistry, Geophysics, Geosystems*, 12, Q07010. <https://doi.org/10.1029/2010GC003450>
- Hsu, Y. J., Simons, M., Avouac, J. P., Galetzka, J., Sieh, K., Chlieh, M., et al. (2006). Frictional afterslip following the 2005 Nias-Simeulue earthquake, Sumatra. *Science*, 312(5782), 1921–1926. <https://doi.org/10.1126/science.1126960>
- Ishii, M., Shearer, P. M., Houston, H., & Vidale, J. E. (2007). Teleseismic *P* wave imaging of the 26 December 2004 Sumatra-Andaman and 28 March 2005 Sumatra earthquake ruptures using the Hi-net array. *Journal of Geophysical Research*, 112, B11307. <https://doi.org/10.1029/2006JB004700>
- Jónsson, S., Segall, P., Pedersen, R., & Björnsson, G. (2003). Post-earthquake ground movements correlated to pore-pressure transients. *Nature*, 424(6945), 179–183. <https://doi.org/10.1038/nature01776>
- Konca, A. O., Avouac, J. P., Sladen, A., Meltzner, A. J., Sieh, K., Fang, P., et al. (2008). Partial rupture of a locked patch of the Sumatra megathrust during the 2007 earthquake sequence. *Nature*, 456(7222), 631–635. <https://doi.org/10.1038/Nature07572>
- Konca, A. O., Hjorleifsdottir, V., Song, T. R. A., Avouac, J. P., Helmberger, D. V., Ji, C., et al. (2007). Rupture kinematics of the 2005 Mw 8.6 Nias-Simeulue earthquake from the joint inversion of seismic and geodetic data. *Bulletin of the Seismological Society of America*, 97(1A), S307–S322. <https://doi.org/10.1785/0120050632>
- Lange, D., Tilmann, F., Rietbrock, A., Collings, R., Natawidjaja, D. H., Suwargadi, B. W., et al. (2010). The fine structure of the subducted Investigator Fracture Zone in Western Sumatra as seen by local seismicity. *Earth and Planetary Science Letters*, 298(1–2), 47–56. <https://doi.org/10.1016/j.epsl.2010.07.020>
- Li, L., Niu, F. L., Chen, Q. F., Su, J. R., & He, J. B. (2017). Post-seismic velocity changes along the 2008 M7.9 Wenchuan earthquake rupture zone revealed by S coda of repeating events. *Geophysical Journal International*, 208(2), 1237–1249. <https://doi.org/10.1093/gji/ggw454>

- Li, Y. G., Chen, P., Cochran, E. S., Vidale, J. E., & Burdette, T. (2006). Seismic evidence for rock damage and healing on the San Andreas fault associated with the 2004  $M 6.0$  Parkfield earthquake. *Bulletin of the Seismological Society of America*, 96(4B), S349–S363. <https://doi.org/10.1785/0120050803>
- Li, Y. G., Vidale, J. E., Aki, K., Xu, F., & Burdette, T. (1998). Evidence of shallow fault zone strengthening after the 1992  $M 7.5$  Landers, California, earthquake. *Science*, 279(5348), 217–219. <https://doi.org/10.1126/science.279.5348.217>
- Lobkis, O. I., & Weaver, R. L. (2003). Coda-wave interferometry in finite solids: Recovery of P-to-S conversion rates in an elastodynamic billiard. *Physical Review Letters*, 90(25), 254302. <https://doi.org/10.1103/PhysRevLett.90.254302>
- Morgan, P. M., Feng, L. J., Meltzner, A. J., Lindsey, E. O., Tsang, L. L. H., & Hill, E. M. (2017). Sibling earthquakes generated within a persistent rupture barrier on the Sunda megathrust under Simeulue Island. *Geophysical Research Letters*, 44, 2159–2166. <https://doi.org/10.1002/2016GL071901>
- Obermann, A., Planès, T., Hadzioannou, C., & Campillo, M. (2016). Lapse-time-dependent coda-wave depth sensitivity to local velocity perturbations in 3-D heterogeneous elastic media. *Geophysical Journal International*, 207(1), 59–66. <https://doi.org/10.1093/gji/ggw264>
- Obermann, A., Planès, T., Larose, E., Sens-Schönfelder, C., & Campillo, M. (2013). Depth sensitivity of seismic coda waves to velocity perturbations in an elastic heterogeneous medium. *Geophysical Journal International*, 194(1), 372–382. <https://doi.org/10.1093/gji/ggt043>
- Park, J., Song, T. R. A., Tromp, J., Okal, E., Stein, S., Roult, G., et al. (2005). Earth's free oscillations excited by the 26 December 2004 Sumatra-Andaman earthquake. *Science*, 308(5725), 1139–1144. <https://doi.org/10.1126/science.1112305>
- Parzen, E. (1962). On estimation of a probability density function and mode. *Annals of Mathematical Statistics*, 33(3), 1065–1076. <https://doi.org/10.1214/aoms/1177704472>
- Peltzer, G., Rosen, P., Rogez, F., & Hudnut, K. (1996). Postseismic rebound in fault step-overs caused by pore fluid flow. *Science*, 273(5279), 1202–1204. <https://doi.org/10.1126/science.273.5279.1202>
- Peng, Z. G., & Ben-Zion, Y. (2006). Temporal changes of shallow seismic velocity around the Karadere-Düzce branch of the North Anatolian fault and strong ground motion. *Pure and Applied Geophysics*, 163(2–3), 567–600. <https://doi.org/10.1007/s00024-005-0034-6>
- Poupinet, G., Ellsworth, W. L., & Frechet, J. (1984). Monitoring velocity variations in the crust using earthquake doublets: An application to the Calaveras Fault, California. *Journal of Geophysical Research*, 89(B7), 5719–5731. <https://doi.org/10.1029/JB089iB07p05719>
- Qiu, Q., Moore, J. D. P., Barbot, S., Feng, L. J., & Hill, E. M. (2018). Transient rheology of the Sumatran mantle wedge revealed by a decade of great earthquakes. *Nature Communications*, 9(1), 995. <https://doi.org/10.1038/s41467-018-03298-6>
- Rivet, D., Campillo, M., Shapiro, N. M., Cruz-Atienza, V., Radiguet, M., Cotte, N., & Kostoglodov, V. (2011). Seismic evidence of nonlinear crustal deformation during a large slow slip event in Mexico. *Geophysical Research Letters*, 38, L08308. <https://doi.org/10.1029/2011GL047151>
- Rubinstein, J. L., & Beroza, G. C. (2004a). Nonlinear strong ground motion in the  $ML 5.4$  Chittenden earthquake: Evidence that preexisting damage increases susceptibility to further damage. *Geophysical Research Letters*, 31, L23614. <https://doi.org/10.1029/2004GL021357>
- Rubinstein, J. L., & Beroza, G. C. (2004b). Evidence for widespread nonlinear strong ground motion in the  $Mw 6.9$  Loma Prieta earthquake. *Bulletin of the Seismological Society of America*, 94(5), 1595–1608. <https://doi.org/10.1785/0120040009>
- Rubinstein, J. L., Uchida, N., & Beroza, G. C. (2007). Seismic velocity reductions caused by the 2003 Tokachi-Oki earthquake. *Journal of Geophysical Research*, 112, B05315. <https://doi.org/10.1029/2006JB004440>
- Sawazaki, K., Kimura, H., Shiomi, K., Uchida, N., Takagi, R., & Snieder, R. (2015). Depth-dependence of seismic velocity change associated with the 2011 Tohoku earthquake, Japan, revealed from repeating earthquake analysis and finite-difference wave propagation simulation. *Geophysical Journal International*, 201(2), 741–763. <https://doi.org/10.1093/gji/ggv014>
- Sawazaki, K., Saito, T., & Shiomi, K. (2018). Shallow temporal changes in S wave velocity and polarization anisotropy associated with the 2016 Kumamoto earthquake sequence, Japan. *Journal of Geophysical Research: Solid Earth*, 123, 9899–9913. <https://doi.org/10.1029/2018JB016261>
- Schaff, D. P., & Beroza, G. C. (2004). Coseismic and postseismic velocity changes measured by repeating earthquakes. *Journal of Geophysical Research*, 109, B10302. <https://doi.org/10.1029/2004JB003011>
- Snieder, R. (2006). The theory of coda wave interferometry. *Pure and Applied Geophysics*, 163(2–3), 455–473. <https://doi.org/10.1007/s00024-005-0026-6>
- Snieder, R., Grêt, A., Douma, H., & Scales, J. (2002). Coda wave interferometry for estimating nonlinear behavior in seismic velocity. *Science*, 295(5563), 2253–2255. <https://doi.org/10.1126/science.1070015>
- Snieder, R., Sens-Schönfelder, C., & Wu, R. J. (2017). The time dependence of rock healing as a universal relaxation process, a tutorial. *Geophysical Journal International*, 208(1), 1–9. <https://doi.org/10.1093/gji/ggw377>
- Subarya, C., Chlieh, M., Prawirodiridjo, L., Avouac, J. P., Bock, Y., Sieh, K., et al. (2006). Plate-boundary deformation associated with the great Sumatra-Andaman earthquake. *Nature*, 440(7080), 46–51. <https://doi.org/10.1038/nature04522>
- Takagi, R., Okada, T., Nakahara, H., Umino, N., & Hasegawa, A. (2012). Coseismic velocity change in and around the focal region of the 2008 Iwate-Miyagi Nairiku earthquake. *Journal of Geophysical Research*, 117, B06315. <https://doi.org/10.1029/2012JB009252>
- Tang, C. H., Hsu, Y. J., Barbot, S., Moore, J. D. P., & Chang, W. L. (2019). Lower-crustal rheology and thermal gradient in the Taiwan orogenic belt illuminated by the 1999 Chi-Chi earthquake. *Science Advances*, 5(2). <https://doi.org/10.1126/sciadv.aav3287>
- TenCate, J. A., Smith, E., & Guyer, R. A. (2000). Universal slow dynamics in granular solids. *Physical Review Letters*, 85(5), 1020–1023. <https://doi.org/10.1103/PhysRevLett.85.1020>
- Tsang, L. L. H., Hill, E. M., Barbot, S., Qiu, Q., Feng, L. J., Hermawan, I., et al. (2016). Afterslip following the 2007  $Mw 8.4$  Bengkulu earthquake in Sumatra loaded the 2010  $Mw 7.8$  Mentawai tsunami rupture zone. *Journal of Geophysical Research: Solid Earth*, 121, 9034–9049. <https://doi.org/10.1002/2016JB013432>
- Vidale, J. E., & Helmberger, D. V. (1988). Elastic finite-difference modeling of the 1971 San Fernando, California earthquake. *Bulletin of the Seismological Society of America*, 78(1), 122–141.
- Vidale, J. E., & Li, Y. G. (2003). Damage to the shallow Landers fault from the nearby Hector Mine earthquake. *Nature*, 421(6922), 524–526. <https://doi.org/10.1038/nature01354>
- Wegler, U., Nakahara, H., Sens-Schönfelder, C., Korn, M., & Shiomi, K. (2009). Sudden drop of seismic velocity after the 2004  $Mw 6.6$  mid-Niigata earthquake, Japan, observed with Passive Image Interferometry. *Journal of Geophysical Research*, 114, B06305. <https://doi.org/10.1029/2008JB005869>
- Wei, S. J., Helmberger, D., & Avouac, J. P. (2013). Modeling the 2012 Wharton basin earthquakes off-Sumatra: Complete lithospheric failure. *Journal of Geophysical Research: Solid Earth*, 118, 3592–3609. <https://doi.org/10.1002/jgrb.50267>
- Wen, L. (2006). Localized temporal change of the Earth's inner core boundary. *Science*, 314(5801), 967–970. <https://doi.org/10.1126/science.1131692>

- Wu, C. Q., Peng, Z. G., & Ben-Zion, Y. (2009). Non-linearity and temporal changes of fault zone site response associated with strong ground motion. *Geophysical Journal International*, 176(1), 265–278. <https://doi.org/10.1111/j.1365-246X.2008.04005.x>
- Yang, C., Li, G., Niu, F., & Ben-Zion, Y. (2019). Significant effects of shallow seismic and stress properties on phase velocities of Rayleigh waves up to 20 s. *Pure and Applied Geophysics*, 176(3), 1255–1267. <https://doi.org/10.1007/s0024-018-2075-7>
- Yu, T., & Hung, S. H. (2012). Temporal changes of seismic velocity associated with the 2006  $M_w$  6.1 Taitung earthquake in an arc-continent collision suture zone. *Geophysical Research Letters*, 39, L12307. <https://doi.org/10.1029/2012GL051970>
- Yu, W. (2013). Shallow-focus repeating earthquakes in the Tonga-Kermadec-Vanuatu subduction zones. *Bulletin of the Seismological Society of America*, 103(1), 463–486. <https://doi.org/10.1785/0120120123>
- Yu, W., Song, T. R. A., & Silver, P. G. (2013a). Temporal velocity changes in the crust associated with the great Sumatra earthquakes. *Bulletin of the Seismological Society of America*, 103(5), 2797–2809. <https://doi.org/10.1785/0120120354>
- Yu, W., Song, T. R. A., & Silver, P. G. (2013b). Repeating aftershocks of the great 2004 Sumatra and 2005 Nias earthquakes. *Journal of Asian Earth Sciences*, 67–68, 153–170. <https://doi.org/10.1016/j.jseaes.2013.02.018>
- Yu, W., & Wen, L. (2012). Deep-focus repeating earthquakes in the Tonga-Fiji subduction zone. *Bulletin of the Seismological Society of America*, 102(4), 1829–1849. <https://doi.org/10.1785/0120110272>
- Yue, H., Lay, T., & Koper, K. D. (2012). En échelon and orthogonal fault ruptures of the 11 April 2012 great intraplate earthquakes. *Nature*, 490(7419), 245–249. <https://doi.org/10.1038/nature11492>
- Zhao, P., & Peng, Z. G. (2009). Depth extent of damage zones around the central Calaveras fault from waveform analysis of repeating earthquakes. *Geophysical Journal International*, 179(3), 1817–1830. <https://doi.org/10.1111/j.1365-246X.2009.04385.x>